

Cosmic ray heating in cool core clusters – I. Diversity of steady state solutions

Svenja Jacob^{1,2}★ and Christoph Pfrommer¹★

¹Heidelberg Institute for Theoretical Studies, Schloss-Wolfsbrunnenweg 35, D-69118 Heidelberg, Germany

²Zentrum für Astronomie der Universität Heidelberg, Astronomisches Recheninstitut, Mönchhofstr. 12-14, D-69120 Heidelberg, Germany

Accepted XXX. Received YYY; in original form ZZZ

ABSTRACT

The absence of large cooling flows in cool core clusters appears to require self-regulated energy feedback by active galactic nuclei but the exact heating mechanism has not yet been identified. Here, we analyse whether a combination of cosmic ray (CR) heating and thermal conduction can offset radiative cooling. To this end, we compile a large sample of 39 cool core clusters and determine steady state solutions of the hydrodynamic equations that are coupled to the CR energy equation. We find solutions that match the observed density and temperature profiles for all our clusters well. Radiative cooling is balanced by CR heating in the cluster centres and by thermal conduction on larger scales, thus demonstrating the relevance of both heating mechanisms. Our mass deposition rates vary by three orders of magnitude and are linearly correlated to the observed star formation rates. Clusters with large mass deposition rates show larger cooling radii and require a larger radial extent of the CR injection function. Interestingly, our sample shows a continuous sequence in cooling properties: clusters hosting radio mini halos are characterized by the largest cooling radii, star formation and mass deposition rates in our sample and thus signal the presence of a higher cooling activity. The steady state solutions support the structural differences between clusters hosting a radio mini halo and those that do not.

Key words: conduction – radiation mechanisms: non-thermal – cosmic rays – galaxies: active – galaxies: clusters: general.

1 INTRODUCTION

The population of galaxy clusters can be divided into cool core (CC) and non-CC clusters. CC clusters are characterized by low entropies and short cooling times in the centre (Cavagnolo et al. 2009; Hudson et al. 2010). Unimpeded radiative cooling results in cooling flows with mass deposition rates of $1000 M_{\odot} \text{ yr}^{-1}$ (see Peterson & Fabian 2006, for a review). In contrast, only a moderate amount of cold gas and star formation is observed, which can be up to two orders of magnitude smaller than the predictions (Peterson & Fabian 2006). In order to solve the emerging cooling flow problem an additional heating mechanism is required that balances radiative cooling.

In the centres of CC clusters, the temperature increases with radius such that the gas at the temperature peak functions as a heat reservoir. The transport of heat to the centres of clusters by means of thermal conduction has been studied

in great detail (e.g. Bertschinger & Meiksin 1986; Bregman & David 1988; Zakamska & Narayan 2003; Guo et al. 2008). Although it is possible to construct solutions in which thermal conduction balances radiative cooling, the required conductivity has to be fine-tuned (Guo & Oh 2008). Moreover, in some clusters such a thermal balance requires a conductivity that exceeds the theoretical maximum, i.e. the *Spitzer* value (Zakamska & Narayan 2003). In addition the solutions are not locally stable on scales larger than the Field length (Kim & Narayan 2003; Soker 2003). Hence, thermal conduction cannot be the sole solution to the cooling flow problem. Nevertheless, it might still play an important role beyond the central region at intermediate cluster radii (Voit 2011).

Another source of energy that is in principle powerful enough to balance cooling is the feedback from the active galactic nucleus (AGN) of the brightest cluster galaxy (see e.g. McNamara & Nulsen 2007, 2012, for reviews). Here, the critical question is how to efficiently couple this energy to the intra-cluster medium (ICM). Various processes have been explored, including mechanical heating by hot bubbles visible in X-ray observations (e.g. Brüggen & Kaiser

★ svenja.jacob@h-its.org (SJ), christoph.pfrommer@h-its.org (CP)

2002; [Gaspari et al. 2012a](#)) as well as viscous dissipation of sound waves ([Ruszkowski et al. 2004](#)). Additionally, the rising AGN bubbles excite gravity modes that decay and thereby generate turbulence. Hence, dissipation of turbulent motions is another possibility for heating the cluster gas (e.g., [Zhuravleva et al. 2014](#)). However, recent X-ray data find a low ratio of turbulent-to-thermal pressure in the Perseus cluster at 4 per cent, thus challenging this scenario since low-velocity turbulence cannot spread far without being regenerated ([Hitomi Collaboration et al. 2016](#)). This result is in line with idealized hydrodynamical simulations, which demonstrate that the conversion of gravity modes into turbulence is very inefficient and transfers less than 1 per cent of the injected AGN energy to turbulence ([Reynolds et al. 2015](#); [Yang & Reynolds 2016b](#)). Moreover, all these mechanisms can only make use of one quarter of the available enthalpy provided that the bubbles are disrupted by Kelvin-Helmholtz instabilities within a few exponential pressure scale heights ([Pfrommer 2013](#)). The remaining enthalpy is most likely contained as internal energy of relativistic particles and magnetic fields inside the lobes, which also modifies the interplay between jets and the cluster medium ([Sijacki et al. 2008](#); [Guo & Mathews 2011](#)). If the CRs are able to escape the bubbles and fill the ICM, they can heat the cluster gas through streaming.

Streaming CRs excite Alfvén waves via the streaming instability ([Kulsrud & Pearce 1969](#); [Skilling 1971](#); see also [Zweibel 2013](#), for a review). The CRs then scatter on these self-excited waves, which limits the macroscopic CR velocity in the rest frame of the gas to approximately the Alfvén speed ([Wiener et al. 2013](#), assuming pressure carrying CRs at GeV energies). This self-confinement can be very efficient since it operates on time-scales of the order of 30 yr, which is much shorter than all other time-scales in the cluster ([Wiener et al. 2013](#); [Zweibel 2013](#)). The wave growth is counteracted by damping mechanisms such as non-linear Landau (NNL) and turbulent damping ([Farmer & Goldreich 2004](#); [Wiener et al. 2013](#)), which leads to an energy transfer from the CRs to the cluster gas ([Wentzel 1971](#); [Guo & Oh 2008](#)).

Importantly, CR heating allows for a self-regulated feedback loop. The CRs that are injected by the central AGN stream outwards and heat the cluster gas. Thereby, the CRs lose energy and become more and more dilute such that radiative cooling eventually starts to predominate. Cooling gas can then fuel the AGN, which launches relativistic jets that accelerate CRs. Once those escape into the ICM, they stream again outwards and provide a source of heat. An important aspect are the involved time-scales: if CR heating was much slower than the involved dynamical processes, it would not be able to efficiently heat the gas. The free fall time-scale for a typical total density of $\rho = 9 \times 10^{-25} \text{ g cm}^{-3}$ is $\tau_{\text{ff}} = \sqrt{3\pi/(32G\rho)} \approx 7 \times 10^7 \text{ yr}$ ([Krumholz 2015](#)). We compare this value to the Alfvén time since CR heating is mediated by Alfvén waves. If we approximate the Alfvén time-scale as $\tau_A = L/v_A$ and use a typical CR pressure scale height of $L = 30 \text{ kpc}$ and a characteristic Alfvén velocity of $v_A = 200 \text{ km s}^{-1}$ (corresponding to a magnetic field of $10 \mu\text{G}$ and $n_e = 0.01 \text{ cm}^{-3}$), this yields $\tau_A \approx 1.5 \times 10^8 \text{ yr}$. Hence, the Alfvén time-scale is of the same order as the free fall time-scale, which demonstrates that CR heating is sufficiently fast to have an impact on dynamical processes. Moreover,

these time-scales are in the range of typical AGN duty cycles of a few times 10^7 yr to a few times 10^8 yr ([Alexander & Leahy 1987](#); [McNamara et al. 2005](#); [Nulsen et al. 2005](#); [Shabala et al. 2008](#)), which is a necessary condition for sufficient replenishment of CRs.

For these reasons, CR heating has the potential to play a significant role in solving the cooling flow problem ([Loewenstein et al. 1991](#); [Guo & Oh 2008](#); [Enßlin et al. 2011](#); [Fujita & Ohira 2011](#); [Fujita et al. 2013](#); [Pfrommer 2013](#)). In particular, there exists a steady state for spherically symmetric models, in which radiative cooling is balanced by CR heating in the central regions and by thermal conduction further out ([Guo & Oh 2008](#)). Unlike thermal conduction, CR heating is locally stable to thermal fluctuations at $kT \sim 1 \text{ keV}$, coincident with the observed temperature floor in some CC clusters ([Pfrommer 2013](#)). Moreover, detailed gamma-ray and radio observations of the Virgo cluster allow for a CR population that prevents cooling in this particular cluster ([Pfrommer 2013](#)).

Steady state solutions are a necessary condition for the viability of a mechanism to prevent cooling flows. There are various steady state solutions for the ICM that include different physical processes in the literature ([Zakamska & Narayan 2003](#); [Guo et al. 2008](#); [Fujita et al. 2013](#)). If only the effects of thermal conduction are considered, steady state solutions exist but the required conductivity needs to be fine-tuned ([Zakamska & Narayan 2003](#)). This situation can be improved by including AGN feedback that is also able to reduce the conductivity to physical values ([Guo et al. 2008](#)). However, [Guo et al. \(2008\)](#) use the “effervescent heating” model by [Begelman \(2001\)](#), which describes AGN feedback by buoyantly rising bubbles.

Motivated by the results of [Guo & Oh \(2008\)](#) and [Pfrommer \(2013\)](#), we explore steady state solutions that simultaneously take into account thermal conduction and CR heating and discuss common characteristics of the solutions. In our companion paper ([Jacob & Pfrommer 2017](#)), we assess the viability of our solutions by comparing the resulting non-thermal radio and gamma-ray emission to observational data. This enables us to put forward an observationally supported scenario for self-regulated feedback heating, in which an individual cluster can either be stably heated, is predominantly cooling or is transitioning from one state to the other.

Previous works considered at most very small cluster samples. This precludes a sound statistical statement about the viability and applicability of the solution to the entire CC population. Hence, we extend our analysis to a considerably larger cluster sample. Here, we are especially interested in clusters in which CRs have already been observed, e.g. in the form of extended radio emission. In a subsample of CC clusters, such emission occurs as radio mini halos (RMHs) with typical radii of only a few hundred kpc in contrast to the $\sim \text{Mpc}$ radio halos of non-CC clusters (see e.g. [Feretti et al. 2012](#), for a review). Thus, we also include those clusters in the sample selection.

This paper is structured as follows. In Section 2, we introduce our cluster sample and determine required properties from observations. The governing equations of our model and our parameter choices are described in Section 3. We discuss our results in Section 4 and conclude in Section 5.

Throughout the paper, we assume a cosmology with $h = 0.7$, $\Omega_m = 0.3$ and $\Omega_\Lambda = 0.7$.

2 SAMPLE

We analyse a total of 39 CC clusters, which are chosen from the Archive of Chandra Cluster Entropy Profile Tables (ACCEPT, Cavagnolo et al. 2009). Here, we explain our selection criteria and perform fits to the temperature data provided by ACCEPT¹. Moreover, we correlate the cooling time at 1 Gyr to the star formation rate (SFR) of the cD galaxy.

2.1 Sample selection

All clusters in our sample are CC clusters that are selected from the ACCEPT catalogue. It provides density and temperature profiles that are obtained from high resolution *Chandra* observations that reach close to the centre of the clusters. As in Cavagnolo et al. (2009), we consider galaxy clusters as CC clusters if the central value of the entropic function K_0 is smaller than 30 keV cm^2 . For K_0 , we use the fit values from Cavagnolo et al. (2009).

Ideally we would like to choose an X-ray flux limited subsample of the ACCEPT clusters such as the extended Highest X-ray FLUX Galaxy Cluster Sample (HIFLUGCS, Reiprich & Böhringer 2002). However, this sample does not contain all clusters with a confirmed RMH, extended diffuse radio emission in the centres of several CC clusters with a size of up to a few hundred kpc. These sources can only be detected if the surface brightness exceeds a limiting value that depends on the noise properties of the observations, and effectively favours more massive clusters at higher redshifts. Nevertheless, we include those clusters in the sample since their non-thermal emission can be directly compared to our model.

Hence, our sample contains all 15 clusters of Giacintucci et al. (2014) that host an RMH. Moreover, we include the CC clusters from the sample of 50 HIFLUGCS clusters with the highest expected gamma-ray emission from pion decay that are also in ACCEPT (Pinzke et al. 2011). This criterion yields 23 clusters for our sample. Moreover, we include 10 clusters with deep *Chandra* data from Vikhlinin et al. (2006). We also add the Virgo cluster and A 2597 due to their role in previous studies in the context of CR heating and steady state solutions in CC clusters (Zakamska & Narayan 2003; Guo et al. 2008; Fujita et al. 2013; Pfrommer 2013). Since some of these clusters are present in more than one of these samples, our final sample consists of 39 galaxy clusters that are listed with some key properties in Table 1.

In Fig. 1, we show cluster masses and redshifts of our sample.² Clusters that host an RMH (shown with blue circles) are the clusters with the highest redshifts in our sample. This is most likely due to a selection bias associated with the limiting surface brightness effect discussed above. The

¹ <http://www.pa.msu.edu/astro/MC2/accept/>

² We use M_{200} as an estimate for the cluster mass, which is the total mass contained in a sphere so that the mean density is 200 times the critical density $\rho_{\text{crit}} = 3H(z)^2/(8\pi G)$ of the universe, where $H(z)$ is the Hubble function and G the gravitational constant.

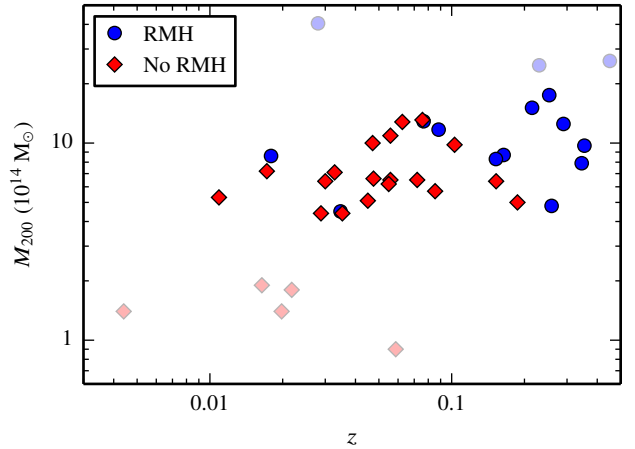


Figure 1. Cluster masses and redshifts of our sample. Clusters with an RMH (blue circles) have typically higher redshifts than clusters without an RMH (red diamonds). The majority of the clusters has comparable masses if we exclude individual clusters at the low and high mass end (shown with transparent colours).

majority of our cluster sample has masses between 4×10^{14} and $2 \times 10^{15} \text{ M}_\odot$, irrespective of whether they host an RMH or not. However, there are five clusters without an RMH that have exceptionally low masses (light red) and three very massive clusters with an RMH (light blue). Where appropriate, we analyse the core sample that is (almost) unbiased in mass and indicate the outliers only for illustrative purposes.

2.2 Temperature profiles

For this work, it is convenient to construct continuous temperature profiles from the ACCEPT data points to find smoother boundary conditions for the integration of the steady state equations and to determine the maximal temperature for each cluster (see Section 3).³ We also use these profiles to determine the cooling time as a function of radius (see Section 2.3).

To describe the temperature profile, we use the model from Allen et al. (2001) with the modifications introduced by Pinzke & Pfrommer (2010) in order to capture the temperature decline at large radii,

$$T = T_0 + (T_1 - T_0) \left[1 + \left(\frac{r}{r_T} \right)^{-\eta} \right]^{-1} \left[1 + \left(\frac{r}{ar_{200}} \right)^2 \right]^{-0.32} \quad (1)$$

with free parameters T_0 , T_1 , r_T and η . We vary the value of a for individual clusters but keep it constant during the fit. The radius r_{200} is defined as the radius corresponding to M_{200} . We use the values for r_{200} from the literature that are

³ Note that ACCEPT temperature profiles are not deprojected. While this may affect steep temperature profiles at small angular scales, the projection effect should not significantly influence our analysis and main conclusions (Vikhlinin et al. 2006; Cavagnolo et al. 2009). We exchange the temperature and density profiles for the Ophiuchus cluster and adopt a weighted average profile of the deprojected sector profiles from Werner et al. (2016), which are based on significantly deeper *Chandra* data.

Table 1. Cluster sample.

Cluster	$z^{(1)}$	$K_0^{(1)}$ keV cm 2	SFR $^{(2)}$ $M_\odot \text{yr}^{-1}$	$r_{200}^{(3)}$ Mpc	$r_{\text{cool}}^{(4)}$ kpc	$M_{200}^{(5)}$ $10^{14} M_\odot$	$M_{200,\text{est}}^{(6)}$ $10^{14} M_\odot$	$v_c^{(6)}$ km s $^{-1}$
Centaurus	0.0109	2.25	0.18 ^a	1.67 ^a	10.9	5.3 ^a	5.7	227
Hydra A	0.0549	13.31	3.77 ^a	1.75 ^a	18.9	6.2 ^a	6.5	326
Virgo (M87)	0.0044	3.53	0.24 ^a	1.08 ^b	9.5	1.4 ^b	3.0	392
A 85	0.0558	12.50	0.61 ^a	2.11 ^a	20.0	10.9 ^a	12.8	261
A 133	0.0558	17.26	...	1.78 ^a	18.7	6.5 ^a	6.1	0
A 262	0.0164	10.57	0.54 ^b	1.17 ^a	5.8	1.9 ^a	2.4	273
A 383	0.1871	13.02	5.58 ^a	1.54 ^c	32.5	5.0 ^c	8.3	346
A 496	0.0328	8.91	...	1.83 ^a	17.0	7.1 ^a	5.4	225
A 539	0.0288	22.59	...	1.56 ^a	2.5	4.4 ^a	3.7	491
A 907	0.1527	23.38	...	1.69 ^c	8.5	6.4 ^c	9.3	250
A 1644	0.0471	19.03	...	2.06 ^a	9.1	10.0 ^a	6.8	0
A 1795	0.0625	18.99	...	2.23 ^a	20.0	12.8 ^a	11.0	0
A 1991	0.0587	1.53	...	0.89 ^c	17.8	0.9 ^c	1.0	323
A 2052	0.0353	9.45	1.4 ^b	1.56 ^a	15.0	4.4 ^a	4.0	0
A 2199	0.0300	13.27	0.58 ^a	1.77 ^a	13.1	6.4 ^a	6.3	323
A 2597	0.0854	10.60	3.23 ^a	1.71 ^a	34.1	5.7 ^a	5.6	319
A 3112	0.0720	11.40	4.2 ^b	1.78 ^a	19.8	6.5 ^a	7.6	336
A 3581	0.0218	9.51	...	1.17 ^a	12.9	1.8 ^a	3.3	207
A 4059	0.0475	7.06	0.57 ^a	1.79 ^a	7.3	6.6 ^a	6.6	233
AWM 7	0.0172	8.37	...	1.84 ^a	5.4	7.2 ^a	4.6	424
MKW3S	0.0450	23.94	...	1.64 ^a	6.6	5.1 ^a	4.4	304
MKW 4	0.0198	6.86	0.03 ^a	1.08 ^a	7.6	1.4 ^a	2.0	364
PKS 0745	0.1028	12.41	17.2 ^b	2.04 ^a	44.5	9.8 ^a	12.0	0
ZwCl 1742	0.0757	23.84	2.02 ^a	2.25 ^a	13.4	13.1 ^a	16.0	0
Ophiuchus*	0.0280	8.95	...	3.28 ^a	13.3	40.5 ^a	16.5	0
Perseus (A 426)	0.0179	19.38	34.46 ^a	1.95 ^a	34.2	8.6 ^a	4.8	0
2A 0335+096	0.0347	7.14	7 ^c	1.58 ^a	31.4	4.5 ^a	5.9	228
A 478	0.0883	7.81	2.39 ^a	2.17 ^a	32.0	11.7 ^a	11.0	358
A 1835	0.2532	11.44	235.37 ^a	2.29 ^d	49.2	17.5 ^d	25.7	0
A 2029	0.0765	10.50	...	2.24 ^a	24.5	12.9 ^a	15.7	531
A 2204	0.1524	9.74	14.7 ^b	1.93 ^a	41.1	8.3 ^a	6.8	463
A 2390	0.2301	14.73	40.6 ^a	2.59 ^d	18.9	24.8 ^d	25.9	0
MS 1455.0+2232	0.2590	16.88	9.46 ^a	1.48 ^c	44.6	4.8 ^c	7.1	569
RBS 0797	0.3540	19.49	...	1.81 ^c	51.5	9.7 ^c	7.8	250
RX J1347.5-1145	0.4510	12.45	...	2.42 ^c	37.8	26.1 ^c	46.3	0
RX J1504.1-0248	0.2150	13.08	140 ^d	2.20 ^c	57.0	15.1 ^c	19.9	0
RX J1532.9+3021	0.3450	16.93	97 ^b	1.70 ^c	51.1	7.9 ^c	11.9	376
RX J1720.1+2638	0.1640	21.03	...	1.87 ^c	32.5	8.7 ^c	12.4	369
ZwCl 3146	0.2900	11.42	65.51 ^a	2.01 ^c	43.8	12.5 ^c	15.0	388

(1) Data are taken from the ACCEPT homepage ([Cavagnolo et al. 2009](#)) except for Ophiuchus (*), for which we use the data from [Werner et al. \(2016\)](#).

(2) a) [Hoffer et al. \(2012\)](#) b) [O'Dea et al. \(2008\)](#) c) [Donahue et al. \(2007\)](#) d) [Ogurian et al. \(2010\)](#)

(3) a) [Pinzke et al. \(2011\)](#) b) [Urban et al. \(2011\)](#) c) r_{500} from [Laganá et al. \(2013\)](#), $r_{200} = r_{500}/0.63$ (see appendix B in [Laganá et al. 2013](#)), d) [Ettori et al. \(2010\)](#)

(4) We define the cooling radius r_{cool} as the radius where the cooling time is 1 Gyr.

(5) a) [Pinzke et al. \(2011\)](#) b) [Urban et al. \(2011\)](#) c) M_{500} from [Laganá et al. \(2013\)](#) d) M_{500} from [Ettori et al. \(2010\)](#), for c) and d), we use $M_{200} = 200 \times 4\pi\rho_{\text{crit}}r_{200}^3/3$.

(6) We use estimates from scaling relations, see Section 3.2.

listed in Table 1. The resulting fit parameters and the maximum radius, out to which the fit is performed, are shown in Table A1.

[Donahue et al. \(2005\)](#), such that

$$\tau_{\text{cool}}(r) = 10^8 \text{ yr} \left[\frac{K(r)}{10 \text{ keV cm}^2} \right]^{3/2} \left[\frac{kT(r)}{5 \text{ keV}} \right]^{-1}, \quad (2)$$

2.3 Cooling time profiles

We use the profile of the cooling time to describe the size of the central region, in which the cooling flow problem is most severe. We determine the cooling time as in

where k is the Boltzmann factor and the quantity $K(r) = kT(r)n_e(r)^{-2/3}$ describes the entropic function as a function

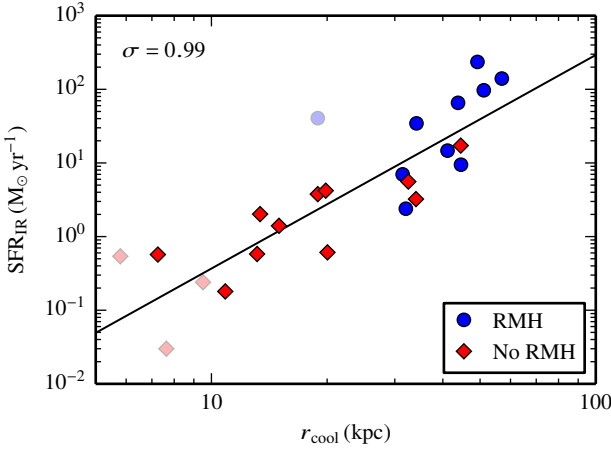


Figure 2. We compare the observed infra-red SFR to the cooling radius, r_{cool} , which is defined as the radius at which the gas has a cooling time of 1 Gyr. The larger the SFR, the larger is also the cooling radius. Clusters hosting an RMH (blue circles) are characterized by large SFRs and cooling radii. Clusters at the low- and high-mass end of our sample are shown with more transparent colours, indicating that the SFR– r_{cool} correlation is not driven by mass. The black line shows a power-law fit to the data of our core sample (shown with full colours) and σ denotes the logarithmic scatter.

of radius with the electron number density n_e . Here, we use the fits for $K(r)$ by Cavagnolo et al. (2009)⁴.

To characterize the cooling time profile, we define the cooling radius r_{cool} as the radius where the cooling time is 1 Gyr. The values for the cooling radius range between 2.5 and 60 kpc (see Table 1 and Fig. 2), which already indicates a substantial variance of cooling properties in our sample. This diversity might be connected to the differences of the inner temperature profiles (Hudson et al. 2010).

In Fig. 2, we compare cooling radii to the observed infra-red SFR. We take the latter from the literature as listed in Table 1. There is a correlation between the SFR and the cooling radius, similar to the results from Hudson et al. (2010). The larger the cooling radius, the larger is also the observed SFR. The black line shows a power-law fit to the data with the log-normal scatter σ . We distinguish between clusters with (blue) and without (red) RMHs. The figure demonstrates that the clusters with the highest SFRs and largest cooling radii host RMHs and vice versa. Moreover, this trend is not primarily driven by mass differences, which indicates another distinction between clusters that is signalled by presence of an RMH and may even be causally connected. We will come back to this correlation in the analysis of the steady state solutions and in the calculation of the non-thermal emission in our companion paper (Jacob & Pfrommer 2017).

⁴ For Ophiuchus, we calculate $K(r)$ from our temperature and density fits (for the density see Jacob & Pfrommer (2017)).

3 THE MODEL

In the following section, we first describe the governing equations for the ICM, explain our approximations and show the resulting steady state equations. Moreover, we specify how the remaining model parameters are chosen.

3.1 Governing equations

Adopting the simplifying assumptions that thermal and CR transport processes are isotropic, the equations for the conservation of mass, momentum, thermal energy and CR energy are given by

$$\frac{d\rho}{dt} + \rho \nabla \cdot \mathbf{v} = 0 \quad (3)$$

$$\frac{d\mathbf{v}}{dt} = -\nabla(P_{\text{th}} + P_{\text{cr}}) - \rho \nabla \phi \quad (4)$$

$$\frac{de_{\text{th}}}{dt} + \gamma_{\text{th}} e_{\text{th}} \nabla \cdot \mathbf{v} = -\nabla \cdot \mathbf{F}_{\text{th}} + \mathcal{H}_{\text{cr}} - \rho \mathcal{L} \quad (5)$$

$$\frac{de_{\text{cr}}}{dt} + \gamma_{\text{cr}} e_{\text{cr}} \nabla \cdot \mathbf{v} = -\nabla \cdot \mathbf{F}_{\text{cr}} - \mathcal{H}_{\text{cr}} + S_{\text{cr}} \quad (6)$$

where $d/dt = \partial/\partial t + \mathbf{v} \cdot \nabla$ denotes the Lagrangian derivative, ρ describes the gas density, \mathbf{v} is the mean gas velocity and ϕ is the gravitational potential. The thermal pressure and energy are given by P_{th} and e_{th} , whereas P_{cr} and e_{cr} specify CR pressure and energy. The conductive heat flux is denoted by \mathbf{F}_{th} , the CR heating rate and radiative cooling rate are denoted by \mathcal{H}_{cr} and $\rho \mathcal{L}$, respectively. F_{cr} and S_{cr} denote the CR streaming flux and CR source function.⁵

We close this set of equations with the equations of state for the thermal gas and the CRs

$$P_{\text{th}} = (\gamma_{\text{th}} - 1)e_{\text{th}} \quad (7)$$

$$P_{\text{cr}} = (\gamma_{\text{cr}} - 1)e_{\text{cr}} \quad (8)$$

where $\gamma_{\text{th}} = 5/3$ is the adiabatic index for a monoatomic gas and $\gamma_{\text{cr}} = 4/3$ is an effective adiabatic index for the CRs, for which we assume the fully relativistic value.

Thermal pressure, gas density and temperature are related by the ideal gas law

$$P_{\text{th}} = \frac{\rho k T}{\mu m_p} = \frac{\mu_e}{\mu} n_e k T \quad (9)$$

with the Boltzmann factor k , the mean molecular weight per particle μ and per electron μ_e . As in Guo et al. (2008) and Zakamska & Narayan (2003), we assume a fully ionized gas with $X = 0.7$ and $Y = 0.28$, such that $\mu = 0.62$ and $\mu_e = 1.18$. Electron and proton number densities are related by $n_e = 1.19 n_p$.

The change in internal energy due to thermal conduction is obtained by the divergence of the conductive heat flux \mathbf{F}_{th} , which in turn is determined by Fourier's law of conduction

$$\mathbf{F}_{\text{th}} = -\kappa \nabla T. \quad (10)$$

The conductivity κ is chosen as a fraction f of the *Spitzer*

⁵ In our model, we adopt the simplifying assumption that we can neglect turbulent heating and diffusive CR transport as a result of scattering off external turbulence (Wiener et al. 2016).

conductivity (Spitzer 1962)

$$\kappa = f \kappa_{\text{sp}} = 1.84 \times 10^{-5} \left(\frac{\ln \lambda}{37} \right)^{-1} f T^{5/2} \text{erg s}^{-1} \text{K}^{-7/2} \text{cm}^{-1}. \quad (11)$$

We describe radiative cooling in the following form:

$$\rho \mathcal{L} = n_e^2 (\Lambda_0 + \Lambda_1 T^{1/2}) \quad (12)$$

where $\Lambda_0 = 1.2 \times 10^{-23} \text{erg s}^{-1} \text{cm}^3$ and $\Lambda_1 = 1.8 \times 10^{-27} \text{erg s}^{-1} \text{cm}^3 \text{K}^{-1/2}$. With this functional form, we approximate the cooling function of Sutherland & Dopita (1993) at solar metallicity, appropriate to the central regions of CCs. In addition to the bremsstrahlung scaling with $T^{1/2}$ at high temperatures, we include the flattening of the cooling function at temperatures below 1 – 2 keV as a result of cooling due to line transitions.

In the self-confinement picture, the CR population propagates with a drift velocity relative to the rest frame of the gas. The drift velocity results from balancing the growth rate of the CR streaming instability and the damping rates due to non-linear Landau (NNL) damping (Kulsrud & Pearce 1969) and turbulent damping (Farmer & Goldreich 2004). NNL damping occurs, when two waves interact and form a beat wave, which propagates with a lower phase speed than the individual waves so that it can interact with thermal particles. Particles that move faster than the beat wave add energy to the wave whereas particles with slower velocities extract wave energy. Since the latter case is typical for a Maxwellian plasma (Wiener et al. 2013), this leads to wave damping. Turbulent damping is caused by pre-existing strong turbulence that causes Alfvén wave packages primarily to decay in the direction that is transverse to the magnetic field. CRs can only resonantly interact with Alfvén waves on their gyro scale. If turbulence causes those waves to decay to smaller scales, the wave growth is exponentially damped (Wiener et al. 2013).

The drift velocity for NNL damping reads for parameters relevant to the centres of CC clusters (Wiener et al. 2013)

$$v_{d,\text{NNL}} = v_A \left(1 + 0.002 \frac{n_{e,-2}^{3/4} (kT_{2\text{keV}})^{1/4}}{B_{10\mu\text{G}} L_{z,20\text{kpc}}^{1/2} n_{\text{cr,fid}}^{1/2}} \gamma^{(\alpha-1)/2} \right), \quad (13)$$

where $n_{e,-2} = n_e/10^{-2} \text{cm}^{-3}$ is the electron number density and $kT_{2\text{keV}} = kT/2 \text{keV}$ is the temperature of CCs, α is the spectral index of the CR proton population, $n_{\text{cr,fid}} = n_{\text{cr}}/8 \times 10^{-9} \text{cm}^{-3}$ is the fiducial CR number density,⁶ $B_{10\mu\text{G}} = B/10\mu\text{G}$ is the magnetic field, $L_{z,20\text{kpc}} = L_z/20 \text{kpc}$ is the CR scale-length and γ denotes the Lorentz factor of CRs. Similarly, if turbulent damping predominates, the CR drift velocity is given by (Wiener et al. 2013)

$$v_{d,\text{turb}} = v_A \left(1 + 0.002 \frac{B_{10\mu\text{G}}^{1/2} n_{e,-2}^{1/2}}{L_{\text{MHD},20\text{kpc}}^{1/2} n_{\text{cr,fid}}} \gamma^{\alpha-3/2} \right), \quad (14)$$

where $L_{\text{MHD},20\text{kpc}} = L_{\text{MHD}}/20 \text{kpc}$ is the length scale at which

⁶ Adopting a power-law CR spectrum with spectral index $\alpha = 2.4$ and low-momentum cutoff $m_{\text{pc}}/2$, the CR number density is $n_{\text{cr}} = 1.3 \times 10^3 P_{\text{cr}}$. To obtain the fiducial CR number density, we assume a CR-to-thermal pressure ratio of 0.1 and values for the thermal pressure as described.

turbulence is excited with velocity perturbations comparable to the Alfvén speed v_A (i.e. with $\mathcal{M}_A = 1$). If velocity perturbations are sub-Alfvénic then we need to extrapolate the wave spectrum to L_{MHD} .

The drift velocity attains contributions from two modes of propagation. The first contribution describes the advection of CRs with the frame of the Alfvén waves that are excited by the streaming instability and we define this velocity as the streaming velocity. Since CRs stream down their pressure gradient (projected on to the local magnetic field), the streaming velocity is given by

$$\mathbf{v}_{\text{st}} = -\text{sgn}(\hat{\mathbf{b}} \cdot \nabla P_{\text{cr}}) \mathbf{v}_A \quad (15)$$

where $\hat{\mathbf{b}}$ denotes the direction of the magnetic field and $\mathbf{v}_A = \mathbf{B}/\sqrt{4\pi\rho}$ is the Alfvén velocity. The subdominant second term in Equations 13 and 14 resembles the CR drift relative to the Alfvén wave frame and depends on plasma conditions and the dominant damping mechanism. Neither of the known damping mechanisms in ionized plasma results in diffusive behaviour. Formally, it can be shown that (Wiener et al. 2013, 2016)

$$\nabla \cdot (\kappa_d \nabla e_{\text{cr}}) \approx \nabla \cdot (e_{\text{cr}} \mathbf{n} (v_d - v_A)) \quad (16)$$

with a diffusion coefficient, κ_d , and a normal vector pointing down the CR energy gradient, \mathbf{n} . In the case of turbulent damping, the expression for $(v_d - v_A)$ is independent of ∇P_{cr} , implying that CR transport is equivalent to streaming at velocity v_D down the CR gradient. For NNL damping, $(v_d - v_A) \propto L_z^{-1/2} \propto (\nabla P_{\text{cr}})^{1/2}$. This is again distinct from diffusion where the flux is proportional to ∇P_{cr} . The CR flux density is given by (e.g. Skilling 1971; Guo & Oh 2008; Pfrommer et al. 2017)

$$\mathbf{F}_{\text{cr}} = (e_{\text{cr}} + P_{\text{cr}}) \mathbf{v}_{\text{st}}. \quad (17)$$

Because CRs are advected with the wave frame and electric fields vanish there, CRs cannot experience an impulsive acceleration and can only scatter in pitch angle. Upon transforming to the rest frame of the gas, there are electric fields associated with the propagating Alfvén waves representing time-varying magnetic fields. This causes an energy transfer from the CRs to the gas, with a volumetric heating rate (Wentzel 1971; Ruszkowski et al. 2017)

$$\mathcal{H}_{\text{cr}} = -\mathbf{v}_{\text{st}} \cdot \nabla P_{\text{cr}}. \quad (18)$$

Since CRs stream down their gradient, this term is always positive. Therefore, the thermal gas is invariably heated at the expense of CR energy that is used to drive the dissipating wave field.

3.2 Model specifications

In order to solve the governing equations, we need to specify the gravitational potential, the magnetic field and the CR source term.

We obtain the gravitational potential by combining the results of Newman et al. (2013), who find that the total mass profile in galaxy clusters is best described by a Navarro-Frenk-White profile (NFW, 1997), with the results by Churazov et al. (2010). They show that the gravitational potential of elliptical galaxies in the cluster centres, especially Virgo, are well described by isothermal spheres. Thus, we

use a superposition of an NFW density profile $\rho_{\text{NFW}}(r) = M_s/[4\pi r(r_s + r)^2]$ and a singular isothermal sphere. The total gravitational potential is then given by

$$\phi(r) = \phi_{\text{NFW}}(r) + \phi_{\text{SIS}}(r) = -\frac{GM_s}{r} \ln\left(1 + \frac{r}{r_s}\right) + v_c^2 \ln\left(\frac{r}{1 \text{ kpc}}\right) \quad (19)$$

with the scaling parameters M_s and r_s of the NFW profile and the circular velocity v_c . As in [Zakamska & Narayan \(2003\)](#), we use the peak value of the temperature profile to determine the parameters M_s and r_s for the NFW profile. We obtain these temperatures either from our fits or, in rare cases, take the ACCEPT data point with the largest value of the radial temperature profile. Then, we use equation 23 in [Afshordi & Cen \(2002\)](#), which is derived from numerical studies by [Evrard et al. \(1996\)](#), to calculate M_{200} and proceed as in [Zakamska & Narayan \(2003\)](#) to obtain M_s . The estimated value for M_{200} is listed in Table 1. To calculate the scale radius r_s , we use the scaling relation by [Maoz et al. \(1997\)](#).

The remaining parameter is the circular velocity, v_c , which describes the normalization of the isothermal sphere. In the radial range that we consider in this work, the SIS is only dominant in the centre of the cluster. Hence, we can use the normalization of the SIS to set the extent of this region. To this end, we define a transition radius, r_t , at which the forces from the SIS and from the NFW profile are equal. We now use this transition radius as a free parameter in our model, which also determines the normalization of the SIS (i.e. v_c).

Fig. 3 illustrates a typical example of our model of the gravitational potential. The top panel shows the potential and the bottom panel the corresponding forces in the radial range that we consider for the steady state solutions. The SIS dominates in the cluster centre and becomes subdominant to the NFW profile towards larger scales. Even at the largest relevant radius for this work, the NFW profile remains the governing potential (while the SIS would start to predominate again at much larger radii). This holds for all clusters in our sample. The bottom panel highlights the definition of the transition radius. Here, we demand that the forces due to the SIS and the NFW profile are equally strong, which fixes the normalization of the SIS.

We do not model the magnetic field and its evolution explicitly but need to parametrize it in order to calculate CR streaming. The strength and orientation of magnetic fields in galaxy clusters are uncertain. Here, we will assume spherical symmetry (see also Section 3.3.1) such that it is sufficient to model the radial magnetic field component as ([Vogt & Enßlin 2005](#); [Kuchar & Enßlin 2011](#))

$$B(r) = B_0 \left(\frac{n_e}{0.01 \text{ cm}^{-3}} \right)^{\alpha_B}. \quad (20)$$

We choose a magnetic field normalization $B_0 = 10 \mu\text{G}$ and a power-law index of $\alpha_B = 0.5$. Those values are of the same order as observed magnetic fields in Virgo and Hydra A ([de Gasperin et al. 2012](#); [Kuchar & Enßlin 2011](#)), but somewhat larger than the assumption by [Pfrommer \(2013\)](#). Our general picture that CRs are injected by the central AGN implies that their number density and pressure decrease with radius. Hence, on large scales the radial component of the streaming velocity will be most relevant and is given by $v_{\text{st}} = v_A$.

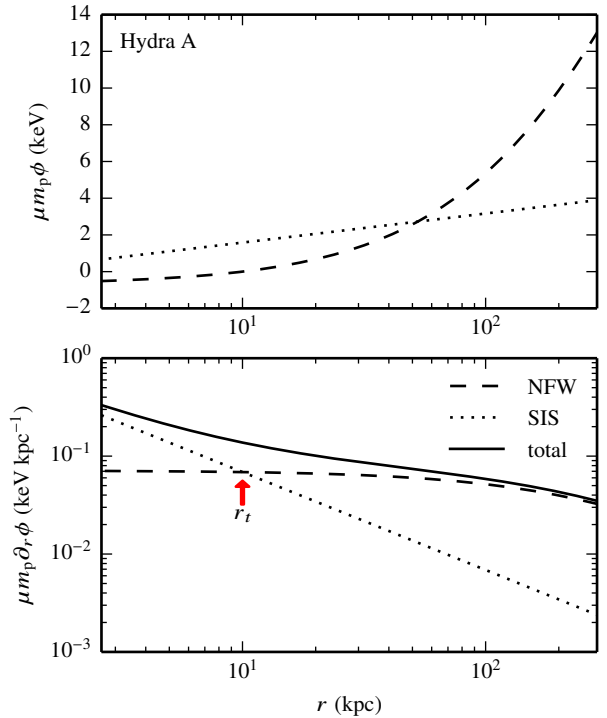


Figure 3. We show our model of the gravitational potential (top) and the corresponding force (bottom) for the cluster Hydra A. The potential is composed of a singular isothermal sphere (SIS) that dominates in the centre and an NFW profile at larger radii. The normalization of the SIS is chosen such that at the radius r_t , the forces of SIS and the NFW profile are equally strong.

In the CR heating term, we also account for small-scale CR pressure fluctuations in addition to the large-scale radial gradients. Fluctuations in the thermal pressure are found by X-ray observations especially in the centre of the cluster. We expect corresponding fluctuations in the CR pressure that also lead to (non-radial) CR streaming and subsequently contribute to the CR heating rate. Following [Pfrommer \(2013\)](#), we model the fluctuations as weak shocks, such that the total CR heating rate is given by

$$\mathcal{H}_{\text{cr}} = -\mathbf{v}_{\text{st}} \cdot \nabla P_{\text{cr}} = -v_A \left(\frac{dP_{\text{cr}}}{dr} - \frac{5}{2} \frac{\varepsilon_f P_{\text{cr}}}{r} \right) \quad (21)$$

where $\varepsilon_f = 0.1$. The first term covers the large-scale radial gradients whereas the second term describes the fluctuations.

To model CR injection, we assume that AGN feedback and thus CR injection are triggered by accretion. Newly injected CRs are first transported inside bubbles to a certain radius r_{cr} and then released. The corresponding source term is given by ([Guo & Oh 2008](#))

$$S_{\text{cr}} = -\frac{\nu \varepsilon_{\text{cr}} \dot{M} c^2}{4\pi r_{\text{cr}}^3} \left(\frac{r}{r_{\text{cr}}} \right)^{-3-\nu} \left(1 - e^{-(r/r_{\text{cr}})^2} \right) \quad (22)$$

where ε_{cr} describes how efficient the rest mass energy of the cooling flow is converted to CR energy, \dot{M} is the mass accretion rate and ν describes the slope of the CR profile after the CRs are released into the ambient medium at the radius r_{cr} . The last factor exponentially suppresses the injection of CRs at radii that are smaller than r_{cr} . We choose $\nu = 0.3$.

as in the fiducial run of [Guo & Oh \(2008\)](#). In the same run, [Guo & Oh \(2008\)](#) choose $r_{\text{cr}} = 20 \text{ kpc}$ and an efficiency of $\varepsilon_{\text{cr}} = 0.003$. Nevertheless, we keep r_{cr} and ε_{cr} as free parameters and take these values only as a first guidance.

3.3 Steady state equations

We obtain the steady state equations from the governing equations in Section 3.1. Here, we introduce the boundary conditions and the selection criteria for the remaining parameters.

3.3.1 Equations

In order to solve Equations (3)-(6), we assume spherical symmetry and only consider a steady state. The simplified equations are given by

$$\dot{M} = 4\pi r^2 \rho v, \quad (23)$$

$$\rho v \frac{dv}{dr} = -\frac{d}{dr}(P_{\text{th}} + P_{\text{cr}}) - \rho \frac{d\phi}{dr}, \quad (24)$$

$$v \frac{de_{\text{th}}}{dr} - \frac{\gamma_{\text{th}} e_{\text{th}} v}{\rho} \frac{d\rho}{dr} = -\frac{1}{r^2} \frac{d}{dr}(r^2 F_{\text{th}}) + \mathcal{H}_{\text{cr}} - \rho \mathcal{L}, \quad (25)$$

$$v \frac{de_{\text{cr}}}{dr} - \frac{\gamma_{\text{cr}} e_{\text{cr}} v}{\rho} \frac{d\rho}{dr} = -\frac{1}{r^2} \frac{d}{dr}(r^2 F_{\text{cr}}) - \mathcal{H}_{\text{cr}} + S_{\text{cr}}, \quad (26)$$

$$F_{\text{th}} = -f \kappa_{\text{sp}} \frac{dT}{dr}. \quad (27)$$

Here, \dot{M} denotes the mass accretion rate through each spherical shell and $F_{\text{cr}} = \gamma_{\text{cr}} e_{\text{cr}} v_A$ the CR flux. We numerically solve the four ordinary differential equations (24) - (27) for the variables $\rho(r)$, $T(r)$, $F_{\text{th}}(r)$ and $P_{\text{cr}}(r)$. The fraction of the *Spitzer* conductivity, f , is treated as an eigenvalue of the problem, which adds a fifth differential equation $df/dr = 0$ to the system of equations. The parameters r_t , \dot{M} , ε_{cr} and r_{cr} are selected prior to the integration according to the criteria presented in Section 3.3.2.

We choose the radius of the innermost ACCEPT data point as the inner boundary r_{in} of the integration. The outer radius r_{out} is chosen such that the temperature fits are still valid and the temperature profile is at most at its maximum since we focus on the centre of the cluster. To solve these five ordinary differential equations, we impose the following five boundary conditions:

$$\rho(r_{\text{in}}) = \rho_{\text{in}}, \quad kT(r_{\text{in}}) = kT_{\text{in}}, \quad (28)$$

$$F_{\text{th}}(r_{\text{in}}) = F_{\text{th,in}}, \quad kT(r_{\text{out}}) = kT_{\text{out}}, \quad (29)$$

$$P_{\text{cr}}(r_{\text{in}}) = P_{\text{cr,in}}. \quad (30)$$

Here, we use the first ACCEPT data point for ρ_{in} .⁷ To determine the temperature values kT_{in} and kT_{out} , we generally use our fitted temperature profiles or, if in some exceptional cases the fits are poor, the corresponding ACCEPT data point. We prefer the smoother fits since the data points can have substantial scatter in the outer regions of the cluster. We do not allow any heat flux to cross the inner boundary and set $F_{\text{th,in}} = 0$ for all clusters. This directly implies that the temperature gradient also vanishes there. We obtain the

⁷ For two clusters (A 3581 and RX J1504), we use the second point instead to avoid an increasing density profile at the centre. For the same reason, we use the maximal value in Perseus.

inner CR pressure $P_{\text{cr,in}}$ by solving the steady state equations at the inner boundary. Since we want to focus on solutions in which CR heating dominates (see also next section), we solve these equations here without the conduction term. All boundary values are also listed in Table 2.

3.3.2 Parameters

The steady state equations still contain four free parameters: r_t , \dot{M} , ε_{cr} and r_{cr} . In order to simplify the integration, we specify these parameters before solving the equations. The values of these parameters can have a significant impact on the solutions. We use this freedom to obtain physical solutions and to focus on CR heating. Therefore, we scan a grid in the parameter space, allowing for all parameter combinations.

The transition radius r_t that links the NFW profile at large scales to that of an isothermal sphere in the centre, assumes values of 0, 5, 10, 20 and 30 kpc. These values allow for a pure NFW profile and reach the maximum size of the central galaxy whose potential might well be described by an isothermal sphere ([Churazov et al. 2010](#)). We adopt a maximum value for the accretion rate of $10 \text{ M}_\odot \text{ yr}^{-1}$ and decrease its value by factors of ten because we aim at solutions without large cooling flows. The efficiency of transforming accreted mass into CR energy, ε_{cr} , varies between 0.001, 0.003, 0.006, 0.01 and 0.03, with a fiducial value of 0.003 ([Guo & Oh 2008](#)). The radius r_{cr} , which describes how far CRs are transported into the ICM by bubbles, varies between 5, 10 and 20 kpc.

From this set of parameters, we choose solutions that fulfil the following criteria. We only accept physical solutions, for which the required fraction of the *Spitzer* conductivity is smaller than unity. The theoretically favoured value is $f \sim 0.3$ or even lower (e.g., [Narayan & Medvedev 2001](#); [Komarov et al. 2016](#)). Moreover, we only accept solutions, whose density and temperature profiles agree well with observations. From the resulting set of solutions, we select those which maximize CR heating. In order to meet constraints from the literature, we require that the central CR-to-thermal pressure value is smaller than 0.3 ([Churazov et al. 2010](#)). Note however, that the required CR pressure also depends on the magnetic field: the larger the magnetic field, the less CRs are necessary to achieve the same amount of heating. As a last criterion, we favour solutions with decreasing CR-to-thermal pressure profiles towards larger radii.

In conclusion, we select parameters that reproduce X-ray observations and make CRs the dominant heat source for a large radial range. The chosen parameters are listed in Table 2.

4 RESULTS

We present and discuss the steady state solutions of our fiducial model with CR and conductive heating for two representative clusters and refer the reader to Appendix A for the remaining part of the sample. In order to understand the impact of CR heating, we additionally explore a straw man's model with conductive heating only. We close this section by analysing the parameter values for our fiducial model that

Table 2. Radial integration limits, boundary conditions and model parameters for our cluster sample.

Cluster	r_{in} kpc	r_{out} kpc	$n_{e,\text{in}}^{(1)}$ cm $^{-3}$	$T_{\text{in}}^{(1)}$ keV	$T_{\text{out}}^{(1)}$ keV	$X_{\text{cr,in}}$	$X_{\text{cr,r}_2}^{(2)}$	$r_{\text{t}}^{(3)}$ kpc	$\dot{M}^{(3)}$ M $_{\odot}$ yr $^{-1}$	$\varepsilon_{\text{cr}}^{(3)}$	$r_{\text{cr}}^{(3)}$ kpc	$f^{(4)}$
Centaurus	0.6	62	0.177	1.0	4.0	0.08	0.03	5	0.1	0.006	5	0.25
Hydra A	2.6	296	0.066	2.8	4.7	0.12	0.07	10	1	0.006	10	0.49
Virgo	0.7	44	0.149	1.9	2.6	0.07	0.07	20	0.1	0.010	5	0.52
A 85	2.6	248	0.086	3.1	7.2	0.14	0.07	5	1	0.010	10	0.27
A 133	2.6	136	0.041	2.3	4.5	0.11	0.05*	0	1	0.003	10	0.43
A 262	0.8	52	0.037	1.5	2.4	0.02	0.02*	10	0.01	0.006	5	0.23
A 383	7.4	156	0.075	3.0	5.6	0.14	0.07*	10	1	0.010	10	0.57
A 496	1.5	79	0.085	2.0	5.4	0.08	0.04*	5	1	0.001	5	0.23
A 539	1.4	38	0.034	3.0	3.3	0.02	0.02	30	0.01	0.010	5	0.12
A 907	6.6	177	0.033	3.6	6.0	0.07	0.06	5	1	0.003	10	0.17
A 1644	2.3	221	0.033	2.1	4.9	0.05	0.03*	0	0.1	0.003	5	0.24
A 1795	2.8	275	0.055	3.3	6.7	0.12	0.07*	0	1	0.006	10	0.42
A 1991	2.7	89	0.102	1.1	2.7	0.15	0.09	20	1	0.003	10	0.55
A 2052	1.7	92	0.038	1.5	3.4	0.08	0.06*	0	1	0.001	10	0.32
A 2199	1.5	84	0.089	2.7	4.6	0.06	0.06*	10	1	0.003	10	0.57
A 2597	3.8	87	0.085	2.4	4.2	0.17	0.06	10	10	0.001	10	0.55
A 3112	3.4	166	0.076	2.7	5.3	0.11	0.06	10	1	0.006	10	0.40
A 3581	1.1	105	0.042	1.4	2.6	0.08	0.03	5	0.1	0.003	5	0.41
A 4059	2.3	140	0.048	2.1	4.8	0.07	0.05	5	0.1	0.006	5	0.19
AWM 7	0.9	78	0.086	2.6	3.8	0.03	0.03*	20	0.1	0.003	5	0.31
MKW 3S	2.2	72	0.036	3.1	3.6	0.04	0.03*	10	0.1	0.010	10	0.80
MKW 4	0.9	43	0.076	1.5	2.1	0.03	0.02*	20	0.01	0.010	5	0.58
PKS 0745	4.5	353	0.112	3.4	12.0	0.24	0.09*	0	10	0.003	10	0.28
ZwCl 1742	3.5	110	0.045	3.0	4.6	0.14	0.09	0	1	0.006	10	0.38
Ophiuchus*	1.2	257	0.234	1.3	8.8	0.18	0.17*	0	1	0.030	20	0.26
Perseus	0.9	114	0.054	3.2	6.5	0.05	0.04*	0	1	0.006	20	0.37
2A 0335	1.6	148	0.120	1.6	4.4	0.22	0.07	5	1	0.010	10	0.67
A 478	4.1	232	0.108	3.1	6.7	0.17	0.07*	10	1	0.006	5	0.58
A 1835	9.4	590	0.117	4.2	11.8	0.21	0.16*	0	10	0.010	20	0.32
A 2029	3.4	264	0.128	4.2	8.5	0.08	0.07*	20	10	0.001	10	0.19
A 2204	6.5	124	0.133	3.3	9.8	0.14	0.09*	20	1	0.030	20	0.15
A 2390	8.7	305	0.065	4.4	11.9	0.11	0.08*	0	10	0.003	20	0.07
MS 1455	9.5	162	0.082	3.6	5.0	0.13	0.08	30	10	0.003	20	0.69
RBS 797	6.2	241	0.096	4.4	9.9	0.22	0.11*	5	10	0.010	20	0.43
RX J1347	14.3	186	0.128	7.7	17.5	0.24	0.15*	0	10	0.030	20	0.14
RX J1504	8.3	537	0.105	4.6	10.0	0.20	0.16*	0	10	0.010	20	0.72
RX J1532	11.6	361	0.093	4.1	7.1	0.23	0.10	10	10	0.010	20	0.94
RX J1720	6.7	287	0.076	4.4	7.3	0.25	0.17	10	10	0.010	20	0.23
ZwCl 3146	10.3	238	0.104	3.8	8.3	0.24	0.11	10	10	0.010	20	0.29

(1) Data are taken from the ACCEPT homepage (Cavagnolo et al. 2009) except for Ophiuchus (★), for which we use the data from Werner et al. (2016).

(2) Values represent our steady state solutions that are evaluated at r_{cool} (no asterisk) or at the radius where CR and conductive heating are equal (denoted by an asterisk, *); see Section 4.1.

(3) These parameters are chosen prior to the integration and kept fixed.

(4) The *Spitzer* fraction for thermal conductivity (f) is treated as an eigenvalue.

give the best-fitting steady state solution with CRs as the dominant heat source.

4.1 Steady state solutions

In Figs. 4 and 5, we show different aspects of the steady state solutions for two example clusters, A 1795 and RX J1720. RX J1720 hosts a confirmed RMH while A 1795 does not.

The top panels of Figs. 4 and 5 show the steady state solutions for the electron number density and temperature. The data points are taken from the ACCEPT sample. Data and steady state solutions agree well for both clusters. Part of the remaining discrepancies could be due to deviations

from our assumptions of a steady state or spherical symmetry. This assumption does not account for features such as the observed bubbles in the central regions of many CC clusters (e.g. Bîrzan et al. 2004). In addition to that, inaccuracies especially in the description of the gravitational potential can have large effects on the resulting density and temperature profiles. Still, we see that the considered physical processes admit steady state solutions that agree well with the observed (azimuthally averaged) thermodynamic profiles.

While this is a necessary requirement for a plausible heating mechanism, it is not sufficient due to potential local and global instabilities. We do not carry out stability anal-

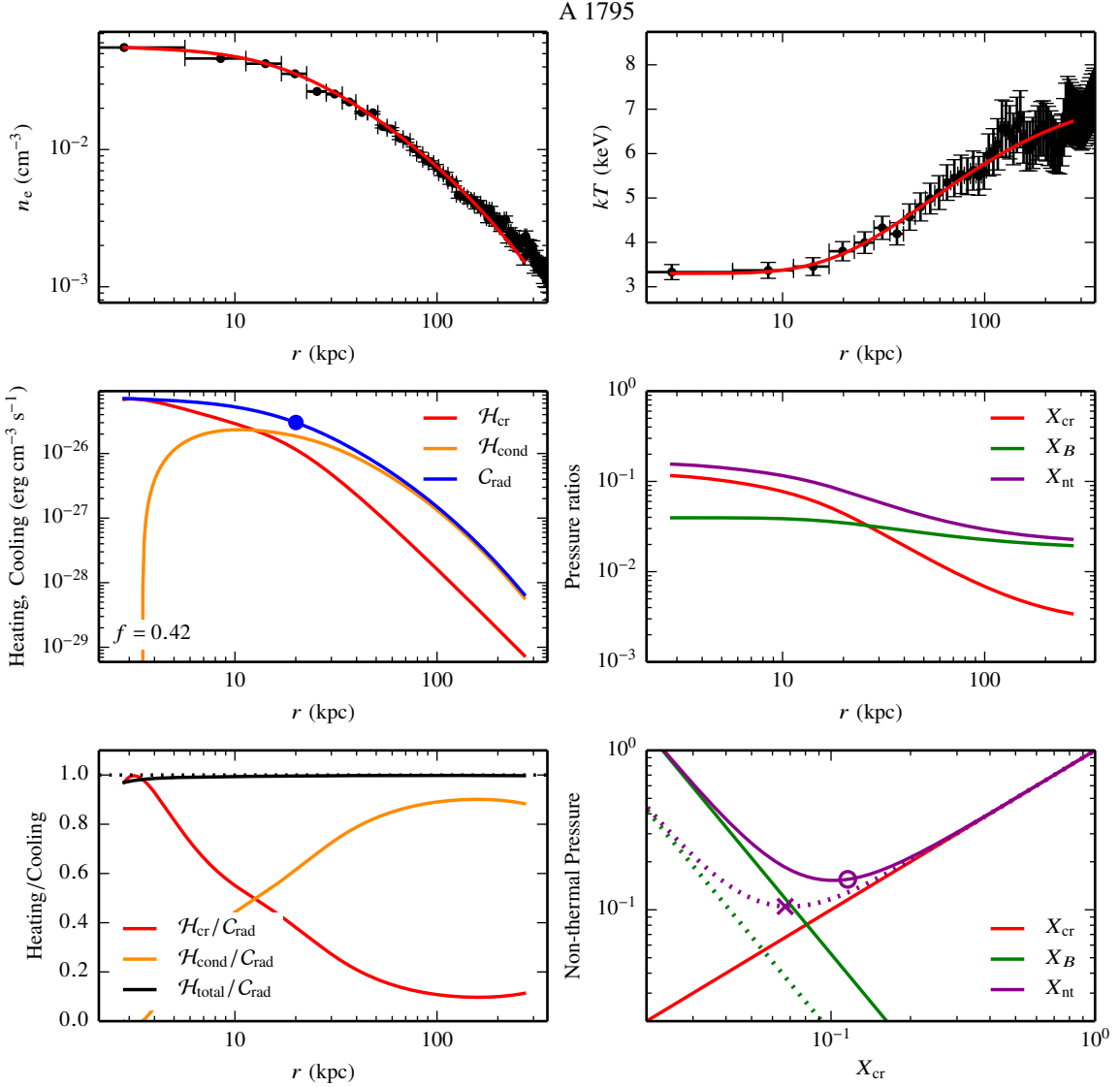


Figure 4. Dissecting the steady state solution for the cluster A 1795. *Top*. Electron number density and temperature profiles. The data points are taken from ACCEPT. *Middle left*. Cooling and heating rates as a function of radius; the filled circle corresponds to the location of the cooling radius. CR heating dominates in the centre of the cluster and thermal conduction becomes more important at larger radii. *Bottom left*. Ratio between the different heating rates to the cooling rate. Note that the total heating-to-cooling ratio (black) is less than unity, indicating a small net cooling that causes mass accretion towards the centre. *Middle right*. Ratios of CR-to-thermal pressure X_{cr} , magnetic-to-thermal pressure X_B , as well as total non-thermal-to-thermal pressure X_{nt} as a function of radius. *Bottom right*. We show the relation between CR pressure and magnetic fields if CR heating balances radiative cooling. The smaller the magnetic field, the more CRs are required and vice versa. The solid lines show the relation at the inner boundary of our solution, the dotted lines correspond to the radius at which CR and conductive heating are equal, as indicated by the cross. The symbols represent the values of the steady state solutions.

yses for our particular set up. However, Pfrommer (2013) demonstrates local stability of CR heating at temperatures $kT \gtrsim 3$ keV, around 1 keV and finds further islands of stability at locations of cooling line complexes in the cooling function. A global stability analysis for CR heating has been carried out by Fujita et al. (2013), who could not find any unstable modes. Guo et al. (2008) show that a combination of thermal conduction and AGN heating can also be globally stable if the AGN feedback is strong enough, thus providing circumstantial evidence that our solutions are likely

sufficiently stable on time-scales relevant for reaching self-regulated heating.

In order to scrutinize the steady state solutions further, we show the relative merits of CR (red) and conductive heating (orange) in comparison to radiative cooling (blue) in the middle-left panels of Figs. 4 and 5 and present both heating rates in units of the cooling rate in the bottom-left panels of these figures. For the chosen set of parameters, CR heating dominates in the centres of the clusters. In A 1795 thermal conduction takes over at ~ 10 kpc, whereas in RX J1720 CR

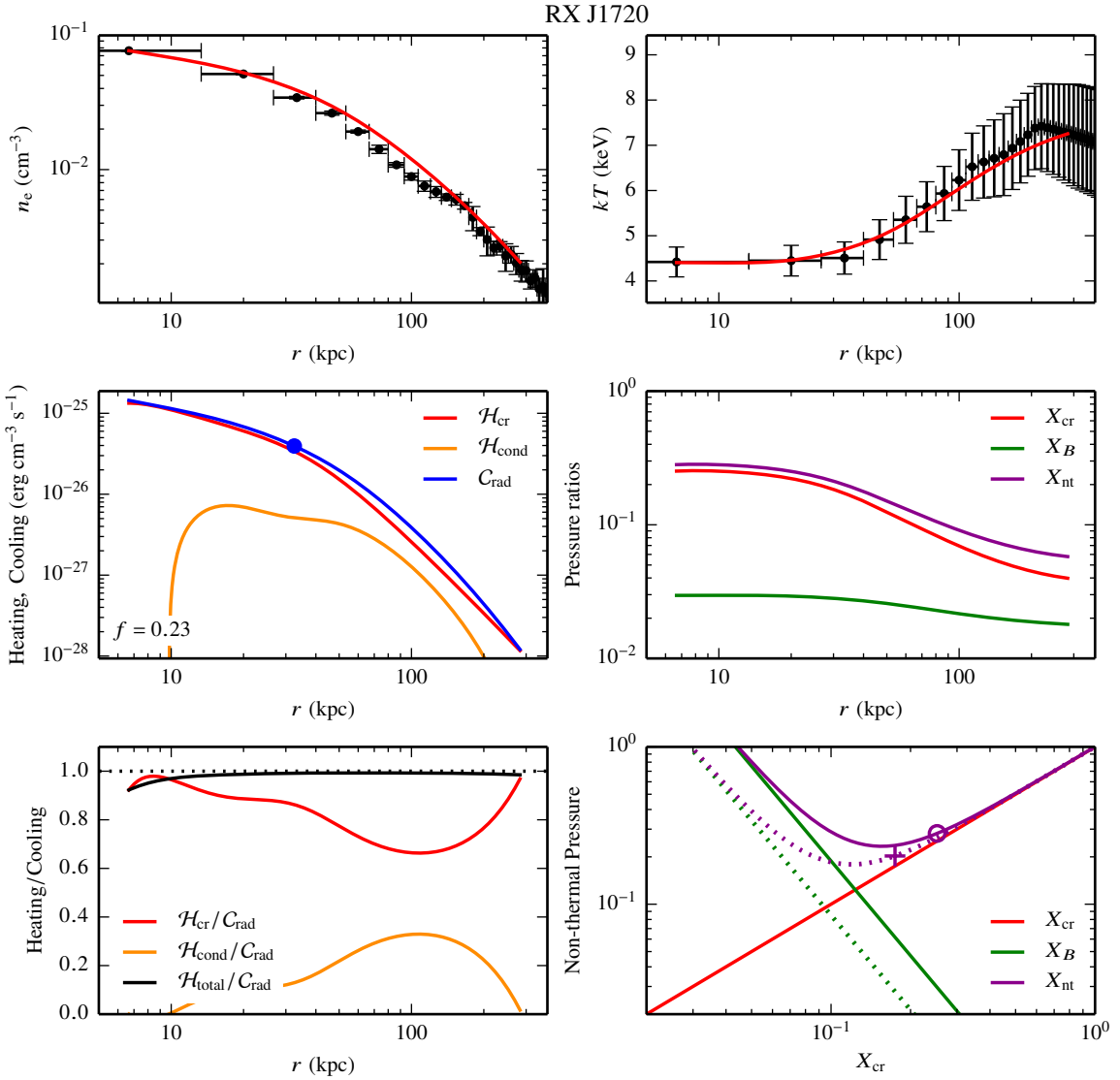


Figure 5. Same as in Fig. 4 but for RX J1720 which hosts an RMH. The plus sign in the bottom-right plot indicates that the dotted lines correspond to the cooling radius.

heating stays dominant over the entire radial range that we consider here. The latter is less typical for the complete sample since thermal conduction usually starts to dominate in the intermediate parts of the cluster, which demonstrates its importance at those radii (see Appendix A). In the middle-left panels of Figs. 4 and 5, we also indicate the required fraction of the *Spitzer* conductivity ($f = 0.42$ and 0.23 for A 1795 and RX J1720, respectively) that will be discussed further in the next section. The solid black line in the bottom-left panels of these figures shows the total heating rate in units of the cooling rate. CR and conductive heating do not exactly add up to the cooling rate because the mass flux (which is by construction constant in each radial shell) and hence the central mass deposition rate are non-zero. As a result, the energy equation contains advection and adiabatic terms that do not vanish (see Equation 25). Moreover, these

terms lead to radial variations of the heating-to-cooling rate ratio.

In the middle-right panel of Figs. 4 and 5, we show radial profiles of the ratio of CR-to-thermal pressure, $X_{\text{cr}} = P_{\text{cr}}/P_{\text{th}}$, and the magnetic-to-thermal pressure ratio, $X_B = B^2/(8\pi P_{\text{th}})$. In both clusters, the CR-to-thermal pressure ratio peaks in the centre and falls off to larger radii as expected for a CR population that is injected by a central AGN. The maximal CR pressure ratio in A 1795 is $X_{\text{cr},\text{max}} \approx 0.10$ and $X_{\text{cr},\text{max}} \approx 0.25$ in RX J1720. Note that the CR-to-thermal pressure ratio is almost constant in the central regions of the clusters and only starts to fall off rapidly beyond the cooling radius. Such a constant pressure ratio is theoretically expected from a steady state where CR heating balances cooling (Pfrommer 2013). This can be seen by estimating the energy per unit volume that is transferred from the CRs

to the thermal gas in steady state,

$$\Delta\varepsilon_{\text{th}} = -\tau_A \mathbf{v}_{\text{st}} \cdot \nabla P_{\text{cr}} \approx P_{\text{cr}} = X_{\text{cr}} P_{\text{th}}, \quad (31)$$

where $\tau_A = \delta l/v_A$ denotes the Alfvén crossing time over a CR pressure gradient length δl .

Fig. 4 also shows that the CR pressure is larger than the magnetic pressure in the centre of A 1795. At larger radii, the CR pressure decreases faster than the magnetic pressure such that the later starts to dominate at a radius of $r \gtrsim 30$ kpc. We see the same trends in RX J1720 (Fig. 5) but there the CR pressure is generally larger and thus stays dominant at all radii.

In this section, we have restricted the discussion to two example clusters but the applicability of our model to the whole sample is a key result of this paper. We present plots similar to Figs. 4 and 5 for the other clusters of our sample in Appendix A. The density and temperature profiles of the steady state solutions in our sample agree well with observations. Radiative cooling is typically balanced in the centre by CR heating and in the intermediate parts of the cluster, closer to the temperature peak, by conductive heating. While the agreement of model and observed thermodynamic variables (such as density and temperature) is a necessary requirement for a viable model, the predicted CR and magnetic pressure values must not conflict with any other observational data. This mainly concerns dynamical potential estimates and non-thermal radio and gamma-ray observations of these clusters. We will return to this point in our companion paper (Jacob & Pfrommer 2017).

4.2 Non-thermal pressure constraints

If CR heating balances radiative cooling as in the cluster centres of our steady state solutions, this imposes further constraints on the non-thermal pressure in the system. Neglecting the mass accretion rate and thermal conduction (which is justified in those regions), we get approximately

$$\begin{aligned} C_{\text{rad},R} \approx \mathcal{H}_{\text{cr},R} &= -v_{A,R} \left(\frac{dP_{\text{cr}}}{dr} \Big|_R - \frac{5}{2} \frac{\varepsilon_f P_{\text{cr},R}}{R} \right) \\ &\approx -v_{A,R} X_{\text{cr}} \left(\frac{dP_{\text{th}}}{dr} \Big|_R - \frac{5}{2} \frac{\varepsilon_f P_{\text{th},R}}{R} \right) \end{aligned} \quad (32)$$

at a given radius R . In the last step, we assume for simplicity that the CR-to-thermal pressure ratio is constant, which is usually a reasonable assumption in the inner parts of the cluster. If temperature and density are known at the radius R , e.g. from observations or from the steady state solutions, the magnetic field that enters implicitly in the Alfvén velocity and X_{cr} remain the only unknown quantities. In this case, Equation (32) implies $BX_{\text{cr}} = \text{const}$ and therefore $X_B \propto X_{\text{cr}}^{-2}$. We use the values for X_B and X_{cr} from the steady state solutions to calculate the constant of proportionality at (i) the inner boundary of the integration, r_{in} , and (ii) either at the cooling radius or at the radius where CR and conductive heating are equal. We choose the smaller of these latter two radii, to avoid that the heating is dominated by conduction. The corresponding CR-to-thermal pressure ratio is also included as X_{cr,r_2} in Table 2.

The bottom-right panels of Figs. 4 and 5 show X_{cr} , X_B and the total non-thermal-to-thermal pressure ratio $X_{\text{nt}} = X_{\text{cr}} + X_B$ as a function of X_{cr} . The solid line corresponds to

the values at the inner boundary, r_{in} , and the circle marks the X_{cr} value that we obtain for our assumptions of the magnetic field. The dotted line indicates the non-thermal pressure at the second radius. A plus sign indicates the use of the cooling radius and the corresponding values of X_{cr} and X_B (see Fig. 5). The cross shows that we use the radius at which CR and conductive heating are equal (see Fig. 4). Independent of the chosen radius, the lower the magnetic pressure, the higher is the required CR pressure to realize the balance between heating and cooling and vice versa. Clearly, the necessary total non-thermal pressure for CR heating to balance cooling reaches a minimum if the magnetic pressure is half the CR pressure. In A 1795, the CR-to-thermal pressure ratios that are realized in our steady state solution are close to this minimum. Hence, the total non-thermal pressure can not be reduced much further in this cluster. In RX J1720, our values lie somewhat above the minimum, especially in the centre of the cluster. However, if the CR pressure is larger than the optimal value, the total non-thermal pressure only increases linearly with X_{cr} .

4.3 CR-to-thermal pressure ratio

How does the CR-to-thermal pressure ratio X_{cr} vary across our sample? In Fig. 6, we show X_{cr} at the inner boundary for each cluster (red circle) and at the outer radius of interest for CR heating. This is the smaller radius of either the cooling radius (at which the radiative cooling time is 1 Gyr) or the radius at which the CR and conductive heating rates are equal. As already discussed in Section 4.1, X_{cr} is approximately constant across the radial range considered and decreases by at most a factor of 3 towards the outer radius (lower panel of Fig. 6). This behaviour is comparable for clusters with and without an RMH.

Most interestingly, the upper panel of Fig. 6 shows that the CR-to-thermal pressure ratio is typically larger in clusters with an RMH in comparison to clusters without an RMH with medians of 0.20 and 0.08, respectively. As we will discuss in more detail in Jacob & Pfrommer (2017), clusters that host an RMH are on average characterized by higher central densities and thus a substantially enhanced cooling rate. To compensate for this increased cooling in steady state, the CR heating rate and thus X_{cr} need to be larger. This is a first indication that the character of the steady state solutions is not uniform across our cluster sample and differs for clusters with and without an RMH.

At first sight, the CR-to-thermal pressure ratios in Fig. 6 appear to be high in comparison to other observational limits on X_{cr} that result e.g., from gamma-ray observations of clusters. However in our model, the CR source is situated at the cluster centre and the CRs lose energy as they stream towards larger radii. This implies a steep radial decline of X_{cr} at radii where CR heating is insufficient to balance cooling and to maintain the thermal pressure profile (equation 31). In cluster centres, the CR pressure can only be probed in tandem with other non-thermal pressure contributions by comparing hydrostatic mass estimates to those inferred by dynamical potential estimates that are probed by orbits of stars and globular clusters (e.g., Churazov et al. 2010). These authors conclude that X_{cr} can reach values of 20 – 30 per cent, which is in agreement with our model. In contrast to that, the upper limits that are derived from the

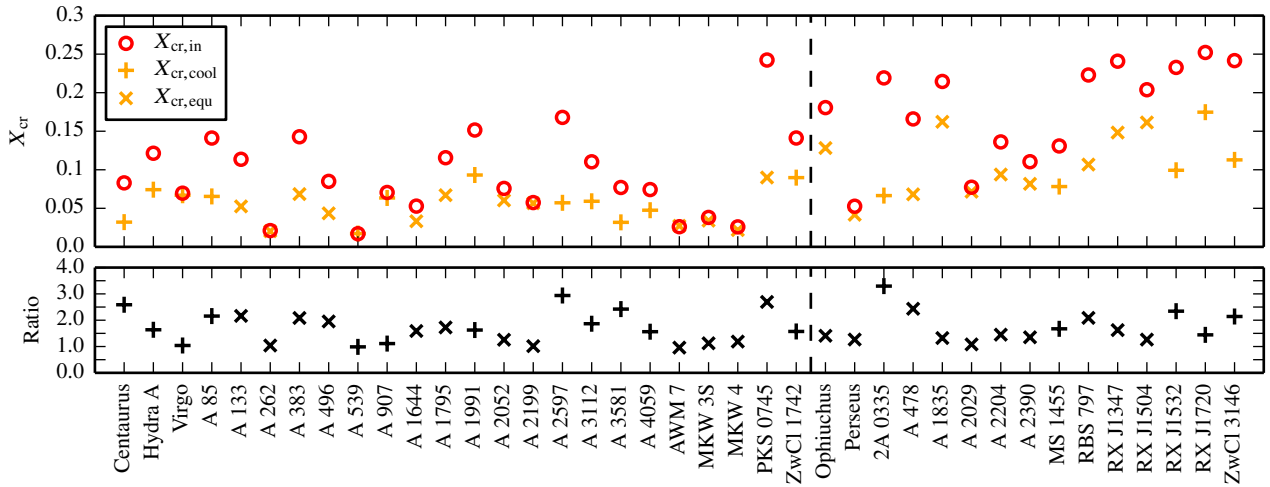


Figure 6. CR-to-thermal pressure ratio X_{cr} at the inner boundary (red circle) and at the outer radius of interest, which is either the cooling radius (+) or the radius at which the CR and conductive heating rates are equal (\times). Absolute values for X_{cr} are shown in the top panel, the bottom panel shows the ratio of X_{cr} at the inner to its value at the outer radius of interest. The steady state solutions in RMH clusters require larger values of X_{cr} in comparison to clusters without RMHs. X_{cr} is approximately constant across the radial range considered and does not significantly differ in both cluster populations.

non-detection of gamma rays typically assume a global CR population that fills the entire cluster out to the virial radius and results from diffusive shock acceleration at cosmological formation shocks (e.g. Ackermann et al. 2014). Due to the large volume that is covered by these models, the allowed X_{cr} values are typically much lower, of the order of 1 – 2 per cent. We emphasize that in order to compare our model with gamma-ray data, we need to compare the predicted (radio and gamma-ray) fluxes with the upper limits from observations. We carry out such an analysis in our companion paper (Jacob & Pfrommer 2017).

4.4 Required fraction of the *Spitzer* conductivity

The ICM is a magnetized and weakly collisional medium. It is characterized by a mean free path that is many orders of magnitudes larger than the Larmor radius. This implies anisotropic transport processes such as thermal conduction to act primarily along the orientation of the local magnetic field and to dramatically change the way in which the ICM responds to perturbations. In the case of a rising temperature profile with radius (which defines cool cores), the heat-flux-driven buoyancy instability (Quataert 2008) might reorient magnetic field lines such that conduction is suppressed in radial direction. Instead, hydrodynamic simulations suggest that turbulence, e.g. from AGN feedback, is able to randomize the magnetic fields (McCourt et al. 2011; Yang & Reynolds 2016a). Moreover, the value of conductivity has been estimated on the basis of observations of steep temperature gradients in the ICM (Ettori & Fabian 2000) and long-lived cold gas that has been stripped from infalling substructure (Eckert et al. 2014). However, these observations can also be explained by magnetic draping, which suppresses thermal conduction and viscosity across these temperature and density gradients by means of a strongly magnetized boundary layer that naturally forms as a result of the magneto-hydrodynamics (Lyutikov 2006; Dursi & Pfrommer

2008; Pfrommer & Jonathan Dursi 2010; Ruszkowski et al. 2014).

The value of the conductivity along the magnetic field is also strongly debated. There is the possibility that mirror instabilities excited by pressure anisotropies can act as magnetic traps for the heat-conducting electrons, suppressing their transport (Komarov et al. 2016; Riquelme et al. 2016) or that oblique whistler modes can resonate with electrons moving in the direction of the heat flux, which potentially causes a suppression of the heat flux (Roberg-Clark et al. 2016). However, the effective volume filling fraction of these processes has not been studied and it is still unclear whether a suppression of the electron transport causes a reduction of the transport of thermal energy.

We treat the fraction of the *Spitzer* conductivity as an eigenvalue of the system of steady state equations. Red crosses in the top panel of Fig. 7 show the *Spitzer* fractions that we obtain from our fiducial solutions. Most of the values lie between 0.2 and 0.6. Note that we directly exclude solutions with $f > 1$ as being unphysical. Still, our values are somewhat on the high side as indicated by the dashed line that represents the isotropic average $f = 0.33$. Nevertheless, considering the ongoing debate about the conductivity in the ICM, so far there is no major problem with our results for f . This result is in line with findings by Voit et al. (2015) who suggest that thermal conduction appears to be important for distinguishing clusters with and without a cool core.

To analyse the impact of CR heating, we also solve the system of hydrodynamic equations without CRs, i.e. Equations (23), (24), (25) and (27). Radiative cooling is then balanced only by thermal conduction, which was already explored by Zakamska & Narayan (2003) and Guo et al. (2008). Unlike these authors, we supplement the gravitational potential of the NFW profile by that of an SIS at small radii, which appears to be required by dynamical potential estimates (Churazov et al. 2010). We use parameters for the gravitational potential (i.e. M_s , r_s , r_t), the mass accretion

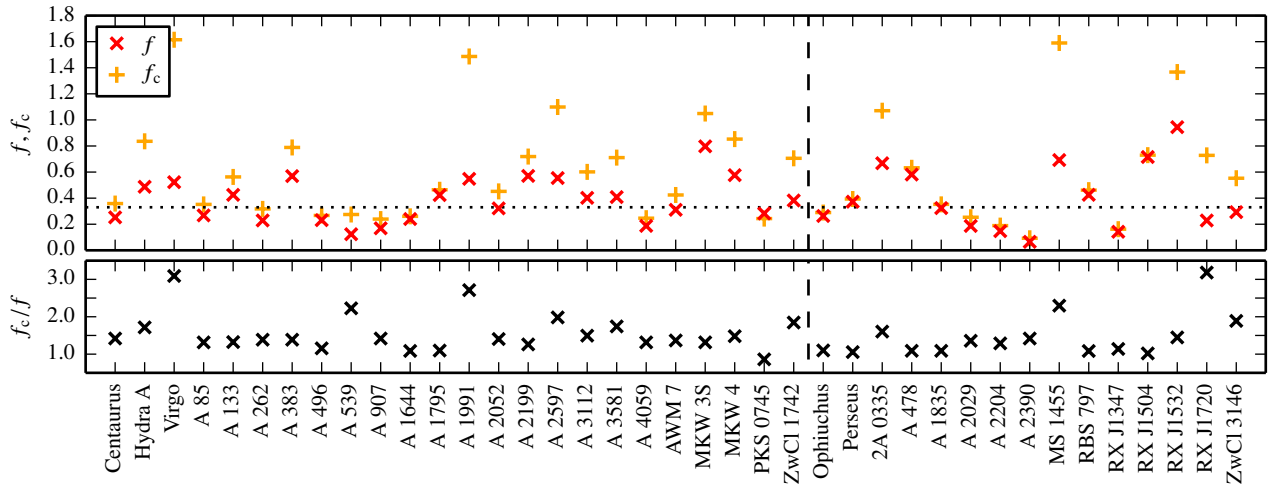


Figure 7. Comparison of the required fraction of the *Spitzer* conductivity in the steady state solutions with (f) and without (f_c) CR heating. The top panel shows the absolute values and the bottom panel the ratio. If CR heating is added, the required value of f is reduced. For some clusters only then $f < 1$ can be achieved, but for most clusters CR heating has a smaller effect on f since thermal conduction still balances radiative cooling on large scales.

rate, the radial range and the boundary conditions that we describe in Section 3.3.1. Without CRs, the temperature and density profiles do not change much since they are primarily determined by the gravitational potential and the boundary conditions.

Interestingly, we obtain different fractions of the *Spitzer* conductivity, denoted as f_c , which are shown in Fig. 7 as orange plus signs. As expected, the required conductivity increases in comparison to the results with CRs since now conduction alone has to balance cooling; in some cases resulting in a conductivity significantly exceeding the *Spitzer* value. Thus, CR heating is required in those clusters to achieve a fraction of the *Spitzer* conductivity that is smaller than unity. The bottom panel in Fig. 7 shows the ratio of the *Spitzer* conductivity with and without CRs. It can be seen that for many clusters the fraction of the *Spitzer* conductivity is not altered dramatically by the addition of CRs, only in rare cases more than a factor of two. The reason is that in both models thermal conduction balances radiative cooling on large scales in many clusters. An example is A 1795, in which the required conductivity remains almost the same. However, if CR heating dominates also on larger scales in our fiducial model, as in our second example cluster RX J1720, the required fraction of the *Spitzer* conductivity is significantly reduced in comparison to the conduction-only case.

Despite the seemingly small effects of CR heating on the steady state solutions, our fiducial model with CR heating has some clear advantages over the model that only includes thermal conduction. First, CR heating is locally stable at certain temperatures in contrast to thermal conduction (Pfrommer 2013). Moreover, CR heating enables a self-regulated AGN feedback loop: CRs are injected by the central AGN and heat the cluster gas by streaming outwards. As soon as the CR population is too dilute and has lost most of its energy, radiative cooling overcomes CR heating such that cold gas can fuel the AGN and trigger CR injection again.

4.5 Parameters for maximal CR heating

The model parameters that enter the steady state equations before integration have a large impact on the solution. Thus, we scrutinize our choice of parameters in this section. To this end, we distinguish between clusters with and without RMHs. Here, we analyse correlations between our parameters and observed quantities and discuss the amount of fine-tuning in our solutions.

We model the gravitational potential as a superposition of a singular isothermal sphere in the centre of the cluster and an NFW profile at larger radii (see also Fig. 3 in Section 3.2). The radius r_t determines the transition between these potentials as it delineates – by construction – equal force contributions by the gravitational potentials of the SIS and the NFW profiles. To justify the usage of an isothermal sphere within the transition radius, we compute the temperature difference between the temperature at the selected transition radius and the inner radius for each cluster. We find that $\Delta T(r_{\text{in}}, r_t) \leq 1$ keV except for one cluster with a temperature difference of 1.7 keV. Assuming quasi-hydrostatic equilibrium, this demonstrates that within r_t an isothermal sphere is a valid assumption for all clusters.

4.5.1 Parameter correlations

In the discussion of our cluster sample, we already pointed out a correlation between the cooling radius and the observed infra-red SFR in Section 2.3. Here, we pursue this topic further and show the most interesting relations between the model parameters as well as between parameters and observations in Fig. 8.

In the left-hand panel of Fig. 8, we compare the observed infra-red SFRs as listed in Table 1 with the mass accretion rates \dot{M} from our steady state solutions. Clusters with high SFRs require higher mass accretion rates to obtain a steady state solution in which CR heating dominates. For visual guidance, the black line shows a linear relation between both quantities, which is consistent with the data.

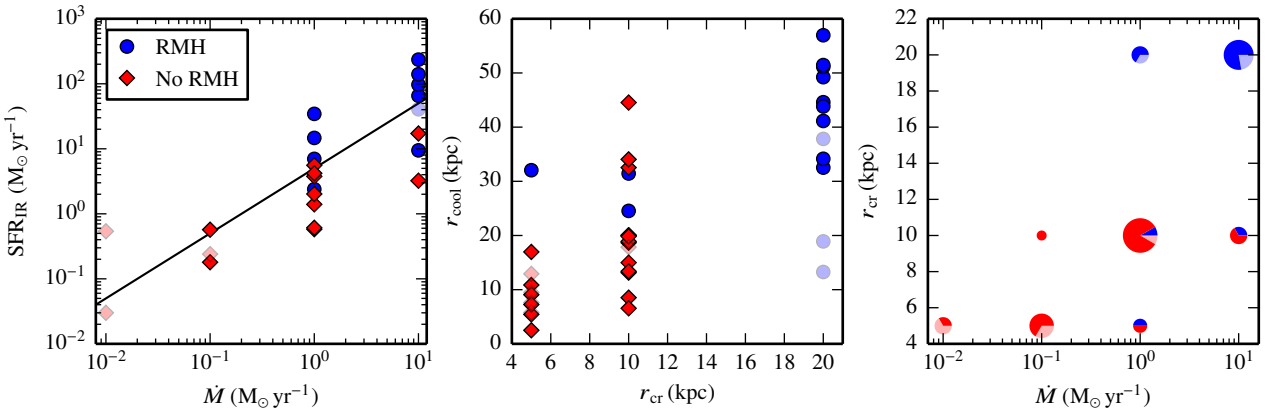


Figure 8. Correlation between model parameters and observed quantities. *Left.* Comparison between observed infra-red SFR and mass accretion rate of our steady state solution. Larger SFRs imply larger mass accretion rates and are more likely to be accompanied by the phenomenon of RMHs. The black line indicates a linear relation between SFRs and \dot{M} . *Middle.* We compare the cooling radius r_{cool} to the CR injection radius r_{cr} . The larger the cooling radius, the larger is the selected CR injection radius, albeit with substantial scatter. Clusters with RMHs have the largest cooling and CR injection radii. *Right.* As a consequence of the other relations, the CR injection radii and mass accretion rates are also correlated.

Apparently, larger mass deposition rates are able to sustain larger SFRs. However, star formation and the mass accretion considered here operate on very different time and length scales, such that a direct link between both is not necessarily expected. Moreover, we note that the SFRs are roughly a factor of 10 higher than the mass accretion rates. Partly this may result from our upper limit of the accretion rate of $\dot{M} = 10 M_{\odot} \text{ yr}^{-1}$. Another possibility is that star formation is triggered by the interaction of AGN jets and the ambient medium (Gaspari et al. 2012b; Li & Bryan 2014; Brighenti et al. 2015). Interestingly, clusters with an RMH have higher observed SFRs and therefore higher values of \dot{M} in comparison to clusters without RMHs.

The middle panel of Fig. 8 shows the relation between the cooling radius r_{cool} as defined in Section 2.3 and the radius r_{cr} in the CR source function. The larger the cooling radius, the larger is the required value of r_{cr} . Such a relation can be expected since a large cooling radius implies that the region where the cooling problem is most severe is also large. In order for CR heating to stably balance radiative cooling, comparably large amounts of CRs are needed in this entire region, which calls for a large CR injection radius r_{cr} . As before, there are differences between the populations of galaxy clusters with and without RMHs: both radii are significantly larger for clusters hosting RMHs.

We finally show the CR injection radius r_{cr} as a function of the mass accretion rate \dot{M} in the right-hand panel in Fig. 8. Since both values are discrete in the parameter grid, points often lie on top of each other. Thus, we indicate the number of the overlying points with the area of the pie chart and the colours show the contributions from clusters with and without RMHs. The smallest pie charts contain only one cluster, whereas the largest chart represents 12 clusters. For the majority of clusters the mass accretion rate correlates well with the CR injection radius, which is a consequence of the relations presented before: larger mass accretion rates imply larger SFRs, which in turn imply larger cooling radii (see Fig. 2) and hence also larger CR injection radii. As expected, clusters hosting an RMH are character-

ized by higher mass accretion rates and larger CR injection radii in comparison to cluster without an RMH.

These correlations are reassuring in that our parameter choices reflect the observed trends and relations of SFR and cooling radius of Fig. 2. Moreover, the relations demonstrate that there is some diversity in the population of CC clusters, with a continuous sequence from cluster hosting an RMH to those without: the latter population shows a smaller SFR and mass accretion rate, which may indicate that CR heating is more efficient in those clusters. Although the smallest mass accretion rates occur in clusters with very low masses, all trends are still clearly visible for the subsample of clusters with similar masses.

4.5.2 Discussion of fine-tuning

The existence of global solutions immediately poses the question of potential fine-tuning of the parameter values. Given the complexity of the involved physics that includes modelling the gravitational potential, the magnetic field and the CR population, a comparably large number of parameters is unavoidable. For some parameters we use values that are common to all clusters. However, we put down a four-dimensional parameter grid in which we are searching for viable solutions.

Due to the diversity in various cluster parameters, such as cooling radius, SFR, and also to a certain extent mass (see Figs. 1 and 2), we do not expect that all their properties can be described by the same universal parameters. Comparable observational constraints among our cluster sample would help to substantiate the parameter choices. However, observations of the magnetic fields or CR populations for such a large cluster sample are not feasible in the near future such that a parametrization of these quantities remains necessary.

Our parameter grid can span orders of magnitude in a parameter value (especially for \dot{M} and ε_{cr}). Hence, our parameter choices represent a range of parameters rather than fine-tuned precise values and we get similarly well matches

to the observational profile if we vary our best-fitting values somewhat. This leads us to the conclusion that although some tuning is indeed required for our solutions, extensive fine-tuning is not necessary.

5 SUMMARY AND CONCLUSIONS

The cooling flow problem in CC clusters remains one of the most interesting open questions in galaxy clusters. While the paradigm of self-regulated AGN feedback is very attractive, the physical heating mechanism that balances radiative cooling has not yet been identified. In this work, we have analysed whether a combination of CR heating and thermal conduction is able to provide the required heating.

To this end, we have compiled one of the largest samples of CC clusters ever used for a theoretical investigation of the cooling flow problem. Here, we have focused on clusters for which non-thermal activity has either already been observed or which are predicted to be suitable targets for non-thermal emission. In particular, this includes all clusters that host a radio mini halo, i.e., an extended radio emission in the centres of the clusters. Clusters with an RMH are typically at slightly higher redshifts than clusters without RMHs, but the virial masses of most clusters are comparable with some outliers that we treat separately. We find that the observed infra-red SFR and the cooling radius, which we define as the radius where the cooling time equals 1 Gyr, are correlated. Moreover, clusters with an RMH have larger SFRs and cooling radii than clusters without RMHs.

For all clusters, we found steady state solutions to the system of hydrodynamic equations coupled to the CR energy equation. The thermal energy equation accounts for thermal conduction as well as Alfvén wave heating excited by streaming CRs. We choose the parameters of the gravitational potential, CR streaming and injection to obtain physical solutions and ask for maximum CR heating solutions. In consequence, we find solutions that match the observed density and temperature profiles well, however requiring a somewhat high conductivity for some systems. Radiative cooling is typically balanced by CR heating in the cluster centres and by thermal conduction in the intermediate cluster parts, closer to the peak in temperature. The combination of these two heating mechanisms has several advantages over models that include only one of the two processes. CR heating is locally stable at temperature values corresponding to islands of stability that form at locations of cooling line complexes in the cooling function (Pfrommer 2013) and it allows for self-regulated AGN feedback, in contrast to thermal conduction, which appears to be nonetheless required to balance cooling at large scales and to allow for mass deposition rates that are in agreement with observational findings.

Our solutions predict modest mass deposition rates; consistent with the low star formation rates and the observed reservoirs of cold gas in the centres of those systems. The cooling gas can escape the detection of soft X-rays ($kT \lesssim 0.5$ keV) by absorption in the filaments with a sufficiently high integrated hydrogen column density and/or by mixing the cooling gas with colder gas, thereby lowering its temperature non-radiatively (Werner et al. 2013, 2014).

Furthermore, we used our comparably large cluster sample to analyse the parameters of these steady state solutions.

We found weak correlations between the observed infra-red SFR and the mass deposition rate in our solutions as well as between the cooling radius and the radial extent of the CR injection. Particularly, clusters with and without RMHs occupy different parts of these relations. Clusters that are hosting an RMH have higher star formation and mass accretion rates in comparison to clusters without an RMH. In addition, the cooling and CR injection radii are typically larger in clusters with an RMH. Hence, the existence of an RMH delineates a homogeneous subclass within the population of CC clusters.

In this work, we present steady state solutions that match X-ray observations well. However, these solutions predict a CR population that interacts hadronically with the ambient medium. As a result, pions are produced which decay into electrons and photons that can be observed in the radio and gamma-ray regime, respectively. The crucial question whether the CR populations of our solutions are in agreement with current observations and upper limits of this non-thermal emission will be addressed in our companion paper (Jacob & Pfrommer 2017).

ACKNOWLEDGEMENTS

We thank Volker Springel for his helpful comments, Norbert Werner for providing the data for the Ophiuchus cluster, and an anonymous referee for a constructive report. SJ acknowledges funding through the graduate college *Astrophysics of cosmological probes of gravity* by Landesgraduiertenakademie Baden-Württemberg. CP acknowledges support by the ERC-CoG grant CRAGSMAN-646955. Both authors have been supported by the Klaus Tschira Foundation.

REFERENCES

- Ackermann M., et al., 2014, *ApJ*, **787**, 18
- Afshordi N., Cen R., 2002, *ApJ*, **564**, 669
- Alexander P., Leahy J. P., 1987, *MNRAS*, **225**, 1
- Allen S. W., Schmidt R. W., Fabian A. C., 2001, *MNRAS*, **328**, L37
- Begelman M. C., 2001, in Laing R. A., Blundell K. M., eds, *Astronomical Society of the Pacific Conference Series* Vol. 250, *Particles and Fields in Radio Galaxies Conference*. p. 443
- Bertschinger E., Meiksin A., 1986, *ApJ*, **306**, L1
- Birzan L., Rafferty D. A., McNamara B. R., Wise M. W., Nulsen P. E. J., 2004, *ApJ*, **607**, 800
- Bregman J. N., David L. P., 1988, *ApJ*, **326**, 639
- Brighenti F., Mathews W. G., Temi P., 2015, *ApJ*, **802**, 118
- Brüggen M., Kaiser C. R., 2002, *Nature*, **418**, 301
- Cavagnolo K. W., Donahue M., Voit G. M., Sun M., 2009, *ApJS*, **182**, 12
- Churazov E., et al., 2010, *MNRAS*, **404**, 1165
- Donahue M., Voit G. M., O'Dea C. P., Baum S. A., Sparks W. B., 2005, *ApJ*, **630**, L13
- Donahue M., Sun M., O'Dea C. P., Voit G. M., Cavagnolo K. W., 2007, *AJ*, **134**, 14
- Dursi L. J., Pfrommer C., 2008, *ApJ*, **677**, 993
- Eckert D., et al., 2014, *A&A*, **570**, A119
- Enblin T., Pfrommer C., Miniati F., Subramanian K., 2011, *A&A*, **527**, A99
- Ettori S., Fabian A. C., 2000, *MNRAS*, **317**, L57

Ettori S., Gastaldello F., Leccardi A., Molendi S., Rossetti M., Buote D., Meneghetti M., 2010, *A&A*, **524**, A68

Evraud A. E., Metzler C. A., Navarro J. F., 1996, *ApJ*, **469**, 494

Farmer A. J., Goldreich P., 2004, *ApJ*, **604**, 671

Feretti L., Giovannini G., Govoni F., Murgia M., 2012, *A&ARv*, **20**, 54

Fujita Y., Ohira Y., 2011, *ApJ*, **738**, 182

Fujita Y., Kimura S., Ohira Y., 2013, *MNRAS*, **432**, 1434

Gaspari M., Brightent F., Temi P., 2012a, *MNRAS*, **424**, 190

Gaspari M., Ruszkowski M., Sharma P., 2012b, *ApJ*, **746**, 94

Giacintucci S., Markevitch M., Venturi T., Clarke T. E., Cassano R., Mazzotta P., 2014, *ApJ*, **781**, 9

Guo F., Mathews W. G., 2011, *ApJ*, **728**, 121

Guo F., Oh S. P., 2008, *MNRAS*, **384**, 251

Guo F., Oh S. P., Ruszkowski M., 2008, *ApJ*, **688**, 859

Hitomi Collaboration et al., 2016, *Nature*, **535**, 117

Hoffer A. S., Donahue M., Hicks A., Barthélémy R. S., 2012, *ApJS*, **199**, 23

Hudson D. S., Mittal R., Reiprich T. H., Nulsen P. E. J., Andernach H., Sarazin C. L., 2010, *A&A*, **513**, A37

Jacob S., Pfrommer C., 2017, *MNRAS*, **467**, 1478

Kim W.-T., Narayan R., 2003, *ApJ*, **596**, 889

Komarov S. V., Churazov E. M., Kunz M. W., Schekochihin A. A., 2016, *MNRAS*,

Krumholz M. R., 2015, preprint, ([arXiv:1511.03457](https://arxiv.org/abs/1511.03457))

Kuchar P., Enßlin T. A., 2011, *A&A*, **529**, A13

Kulsrud R., Pearce W. P., 1969, *ApJ*, **156**, 445

Laganá T. F., Martinet N., Durret F., Lima Neto G. B., Maughan B., Zhang Y.-Y., 2013, *A&A*, **555**, A66

Li Y., Bryan G. L., 2014, *ApJ*, **789**, 153

Loewenstein M., Zweibel E. G., Begelman M. C., 1991, *ApJ*, **377**, 392

Lyutikov M., 2006, *MNRAS*, **373**, 73

Maoz D., Rix H.-W., Gal-Yam A., Gould A., 1997, *ApJ*, **486**, 75

McCourt M., Parrish I. J., Sharma P., Quataert E., 2011, *MNRAS*, **413**, 1295

McNamara B. R., Nulsen P. E. J., 2007, *ARA&A*, **45**, 117

McNamara B. R., Nulsen P. E. J., 2012, *New Journal of Physics*, **14**, 050523

McNamara B. R., Nulsen P. E. J., Wise M. W., Rafferty D. A., Carilli C., Sarazin C. L., Blanton E. L., 2005, *Nature*, **433**, 45

Narayan R., Medvedev M. V., 2001, *ApJ*, **562**, L129

Navarro J. F., Frenk C. S., White S. D. M., 1997, *ApJ*, **490**, 493

Newman A. B., Treu T., Ellis R. S., Sand D. J., Nipoti C., Richard J., Jullo E., 2013, *ApJ*, **765**, 24

Nulsen P. E. J., McNamara B. R., Wise M. W., David L. P., 2005, *ApJ*, **628**, 629

O'Dea C. P., et al., 2008, *ApJ*, **681**, 1035

Ogrean G. A., Hatch N. A., Simionescu A., Böhringer H., Brüggen M., Fabian A. C., Werner N., 2010, *MNRAS*, **406**, 354

Peterson J. R., Fabian A. C., 2006, *Phys. Rep.*, **427**, 1

Pfrommer C., 2013, *ApJ*, **779**, 10

Pfrommer C., Jonathan Dursi L., 2010, *Nature Physics*, **6**, 520

Pfrommer C., Pakmor R., Schaal K., Simpson C. M., Springel V., 2017, *MNRAS*, **465**, 4500

Pinzke A., Pfrommer C., 2010, *MNRAS*, **409**, 449

Pinzke A., Pfrommer C., Bergström L., 2011, *Phys. Rev. D*, **84**, 123509

Quataert E., 2008, *ApJ*, **673**, 758

Reiprich T. H., Böhringer H., 2002, *ApJ*, **567**, 716

Reynolds C. S., Balbus S. A., Schekochihin A. A., 2015, *ApJ*, **815**, 41

Riquelme M. A., Quataert E., Verscharen D., 2016, *ApJ*, **824**, 123

Roberg-Clark G. T., Drake J. F., Reynolds C. S., Swisdak M., 2016, *ApJ*, **830**, L9

Ruszkowski M., Brüggen M., Begelman M. C., 2004, *ApJ*, **611**, 158

Ruszkowski M., Brüggen M., Lee D., Shin M.-S., 2014, *ApJ*, **784**, 75

Ruszkowski M., Yang H.-Y. K., Zweibel E., 2017, *ApJ*, **834**, 208

Shabala S. S., Ash S., Alexander P., Riley J. M., 2008, *MNRAS*, **388**, 625

Sijacki D., Pfrommer C., Springel V., Enßlin T. A., 2008, *MNRAS*, **387**, 1403

Skilling J., 1971, *ApJ*, **170**, 265

Soker N., 2003, *MNRAS*, **342**, 463

Spitzer L., 1962, *Physics of Fully Ionized Gases*

Sutherland R. S., Dopita M. A., 1993, *ApJS*, **88**, 253

Urban O., Werner N., Simionescu A., Allen S. W., Böhringer H., 2011, *MNRAS*, **414**, 2101

Vikhlinin A., Kravtsov A., Forman W., Jones C., Markevitch M., Murray S. S., Van Speybroeck L., 2006, *ApJ*, **640**, 691

Vogt C., Enßlin T. A., 2005, *A&A*, **434**, 67

Voit G. M., 2011, *ApJ*, **740**, 28

Voit G. M., Donahue M., Bryan G. L., McDonald M., 2015, *Nature*, **519**, 203

Wentzel D. G., 1971, *ApJ*, **163**, 503

Werner N., et al., 2013, *ApJ*, **767**, 153

Werner N., et al., 2014, *MNRAS*, **439**, 2291

Werner N., et al., 2016, *MNRAS*, **460**, 2752

Wiener J., Oh S. P., Guo F., 2013, *MNRAS*, **434**, 2209

Wiener J., Pfrommer C., Oh S. P., 2016, preprint, ([arXiv:1608.02585](https://arxiv.org/abs/1608.02585))

Yang H.-Y. K., Reynolds C. S., 2016a, *ApJ*, **818**, 181

Yang H.-Y. K., Reynolds C. S., 2016b, *ApJ*, **829**, 90

Zakamska N. L., Narayan R., 2003, *ApJ*, **582**, 162

Zhuravleva I., et al., 2014, *Nature*, **515**, 85

Zweibel E. G., 2013, *Physics of Plasmas*, **20**, 055501

de Gasperin F., et al., 2012, *A&A*, **547**, A56

APPENDIX A: ADDITIONAL TABLES AND FIGURES

We show the fit parameters for the temperature profile in Table A1. Figs. A1 - A13 show various aspects of the steady state solutions by analogy to Figs. 4 and 5 (albeit in a different order) for the remaining clusters in our sample. The clusters are ordered as in Table 1. The density and temperature data for Ophiuchus are weighted averages of the sector profiles provided by Werner et al. (2016).

This paper has been typeset from a *TeX/LaTeX* file prepared by the author.

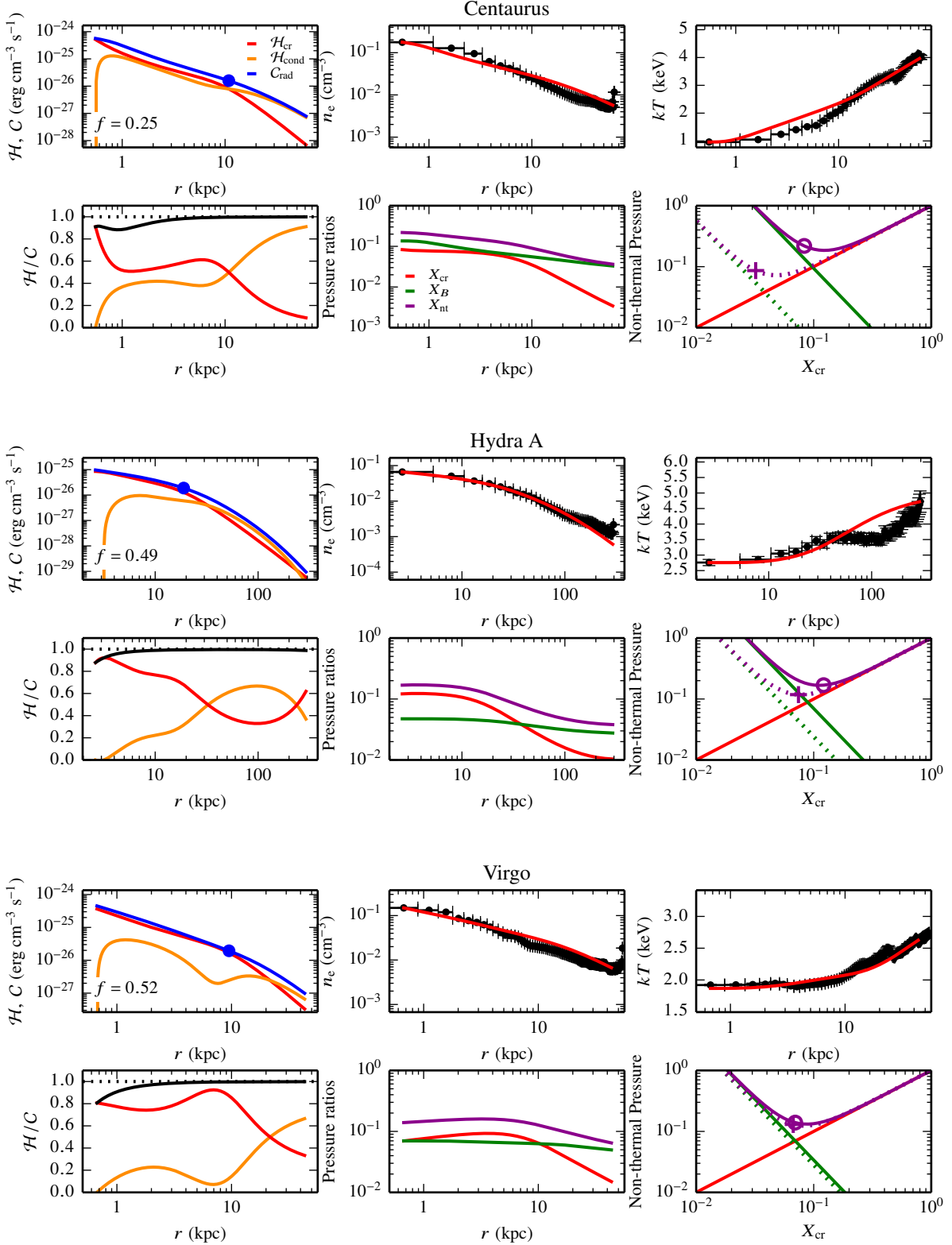


Figure A1. We show the same properties of the steady state solutions as in Fig. 4 for different clusters.

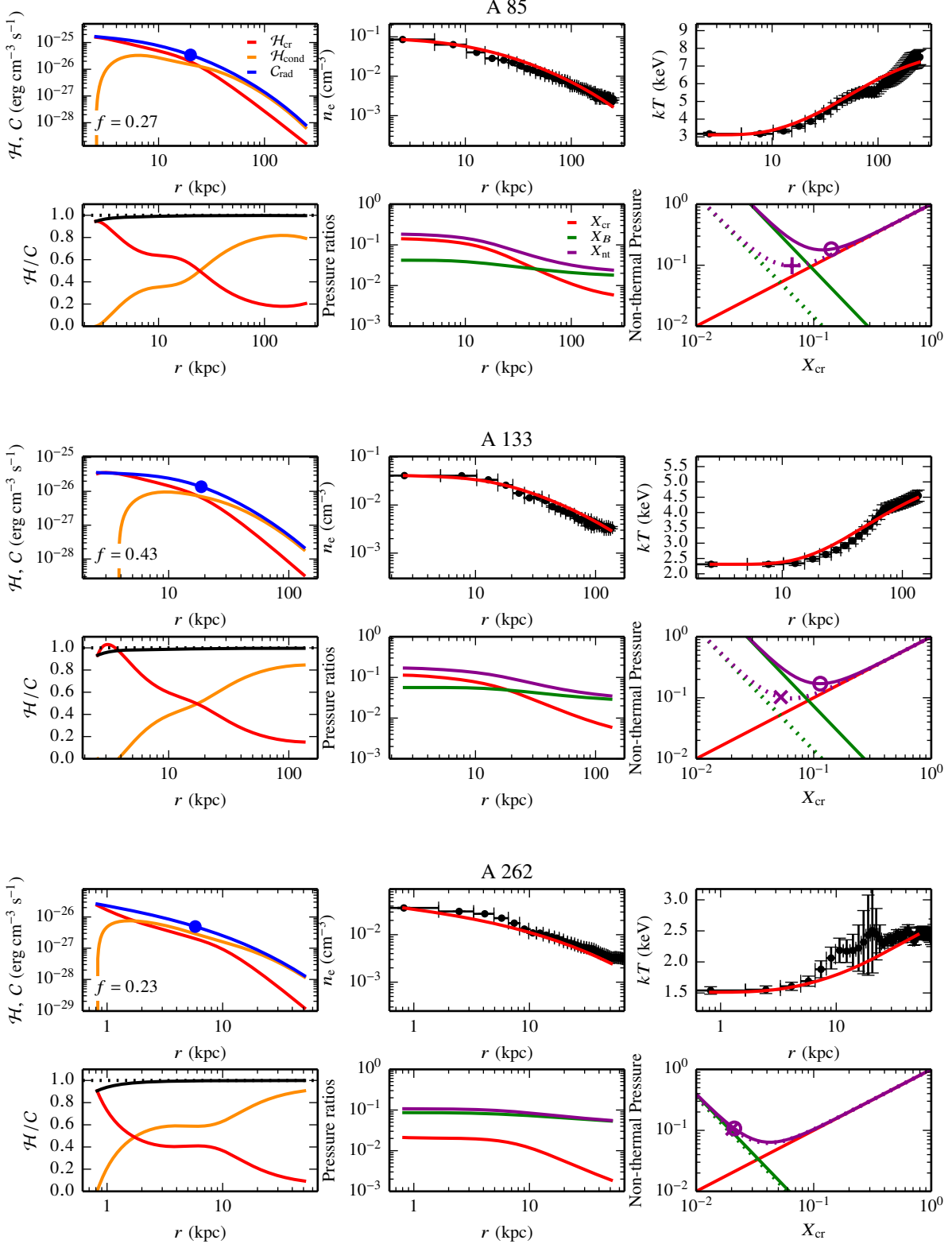


Figure A2. We show the same properties of the steady state solutions as in Fig. 4 for different clusters.

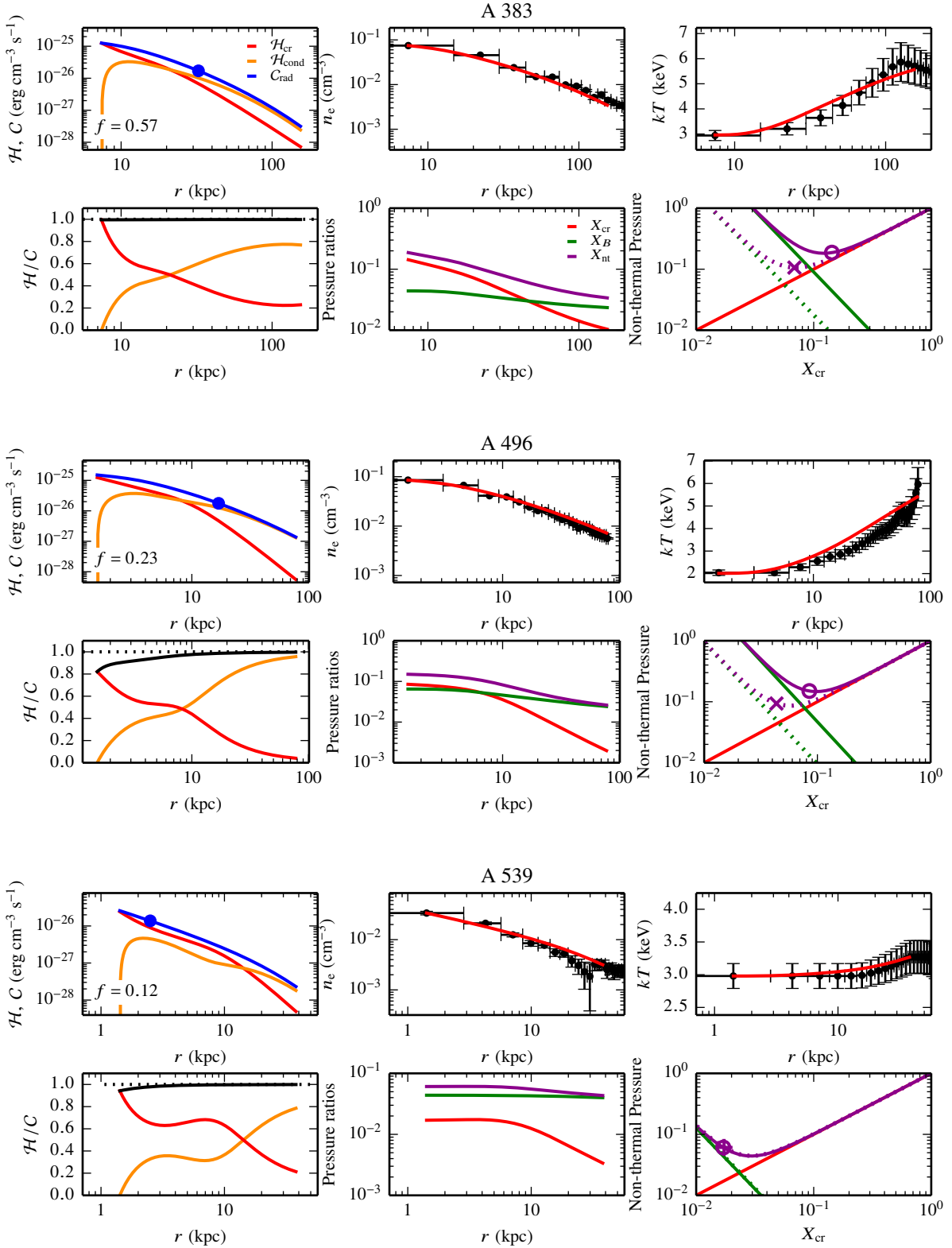


Figure A3. We show the same properties of the steady state solutions as in Fig. 4 for different clusters.

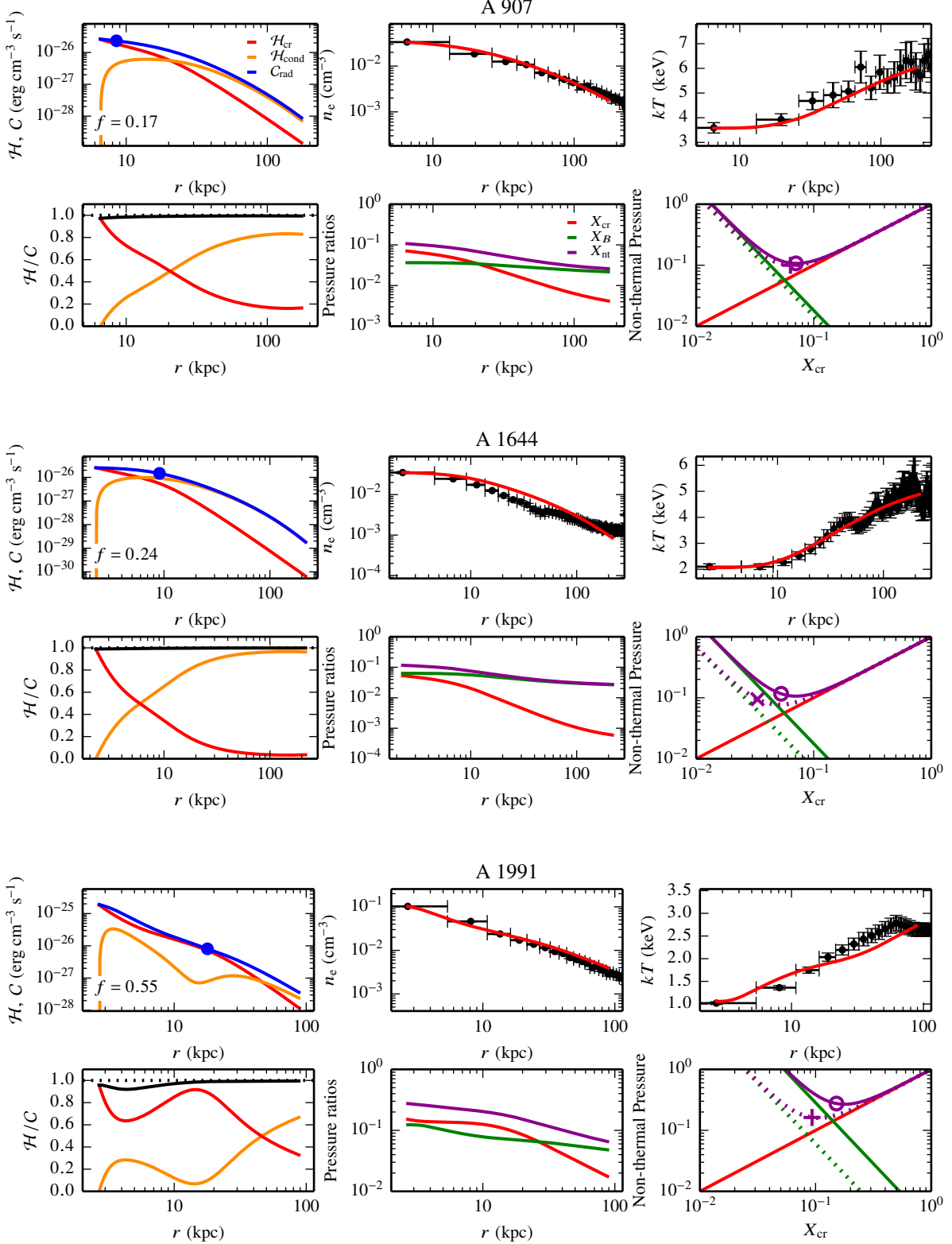


Figure A4. We show the same properties of the steady state solutions as in Fig. 4 for different clusters.

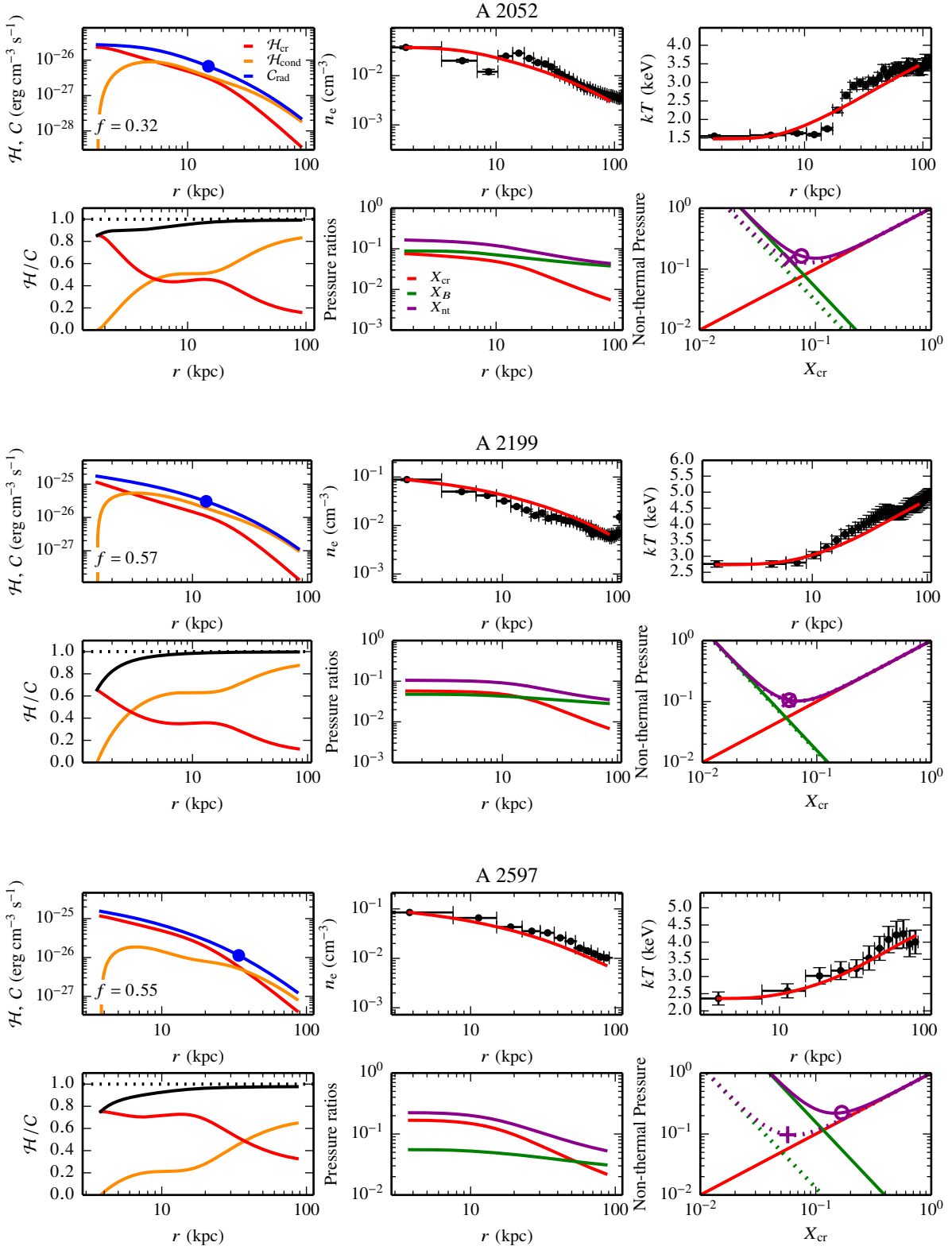


Figure A5. We show the same properties of the steady state solutions as in Fig. 4 for different clusters.

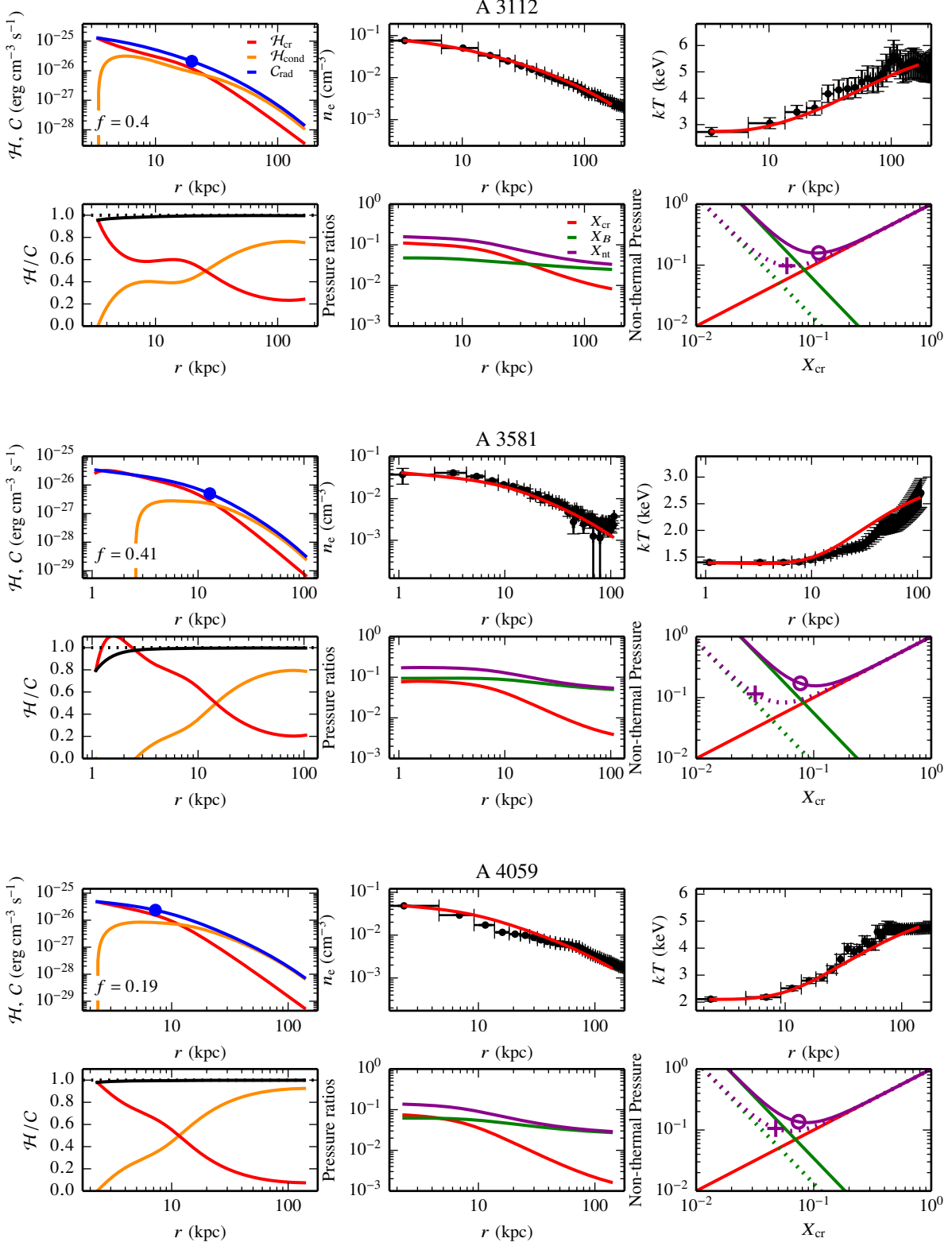


Figure A6. We show the same properties of the steady state solutions as in Fig. 4 for different clusters.

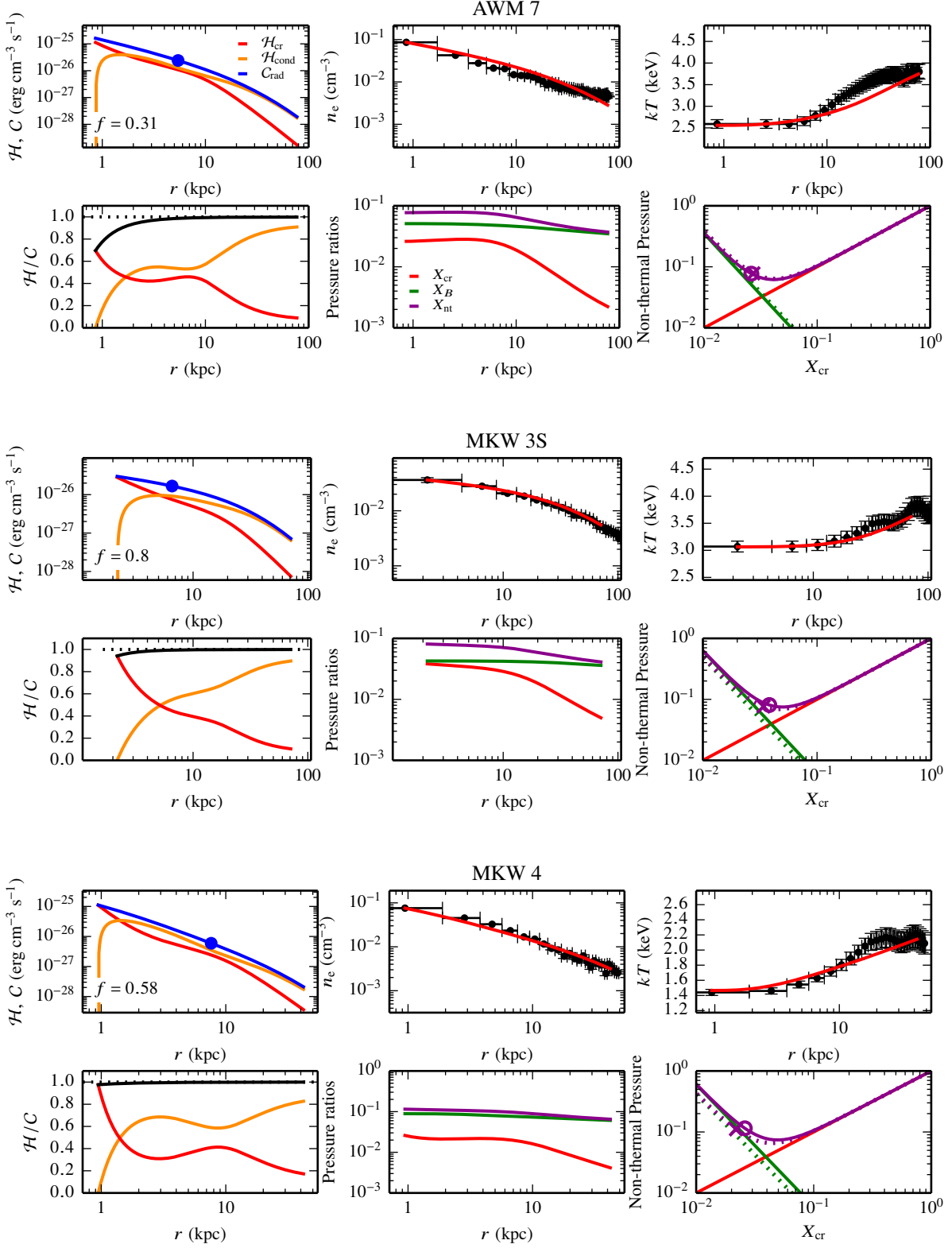


Figure A7. We show the same properties of the steady state solutions as in Fig. 4 for different clusters.

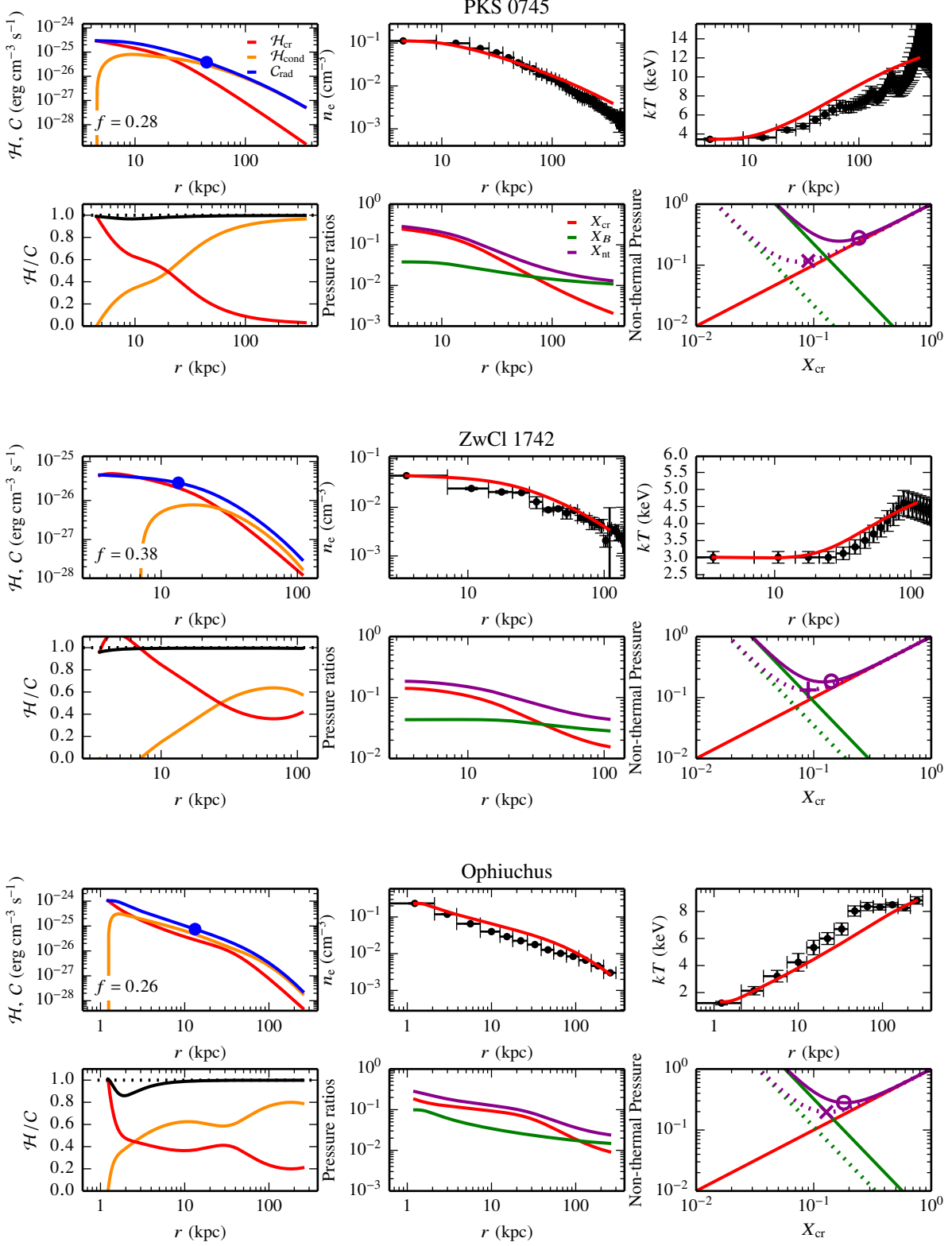


Figure A8. We show the same properties of the steady state solutions as in Fig. 4 for different clusters.

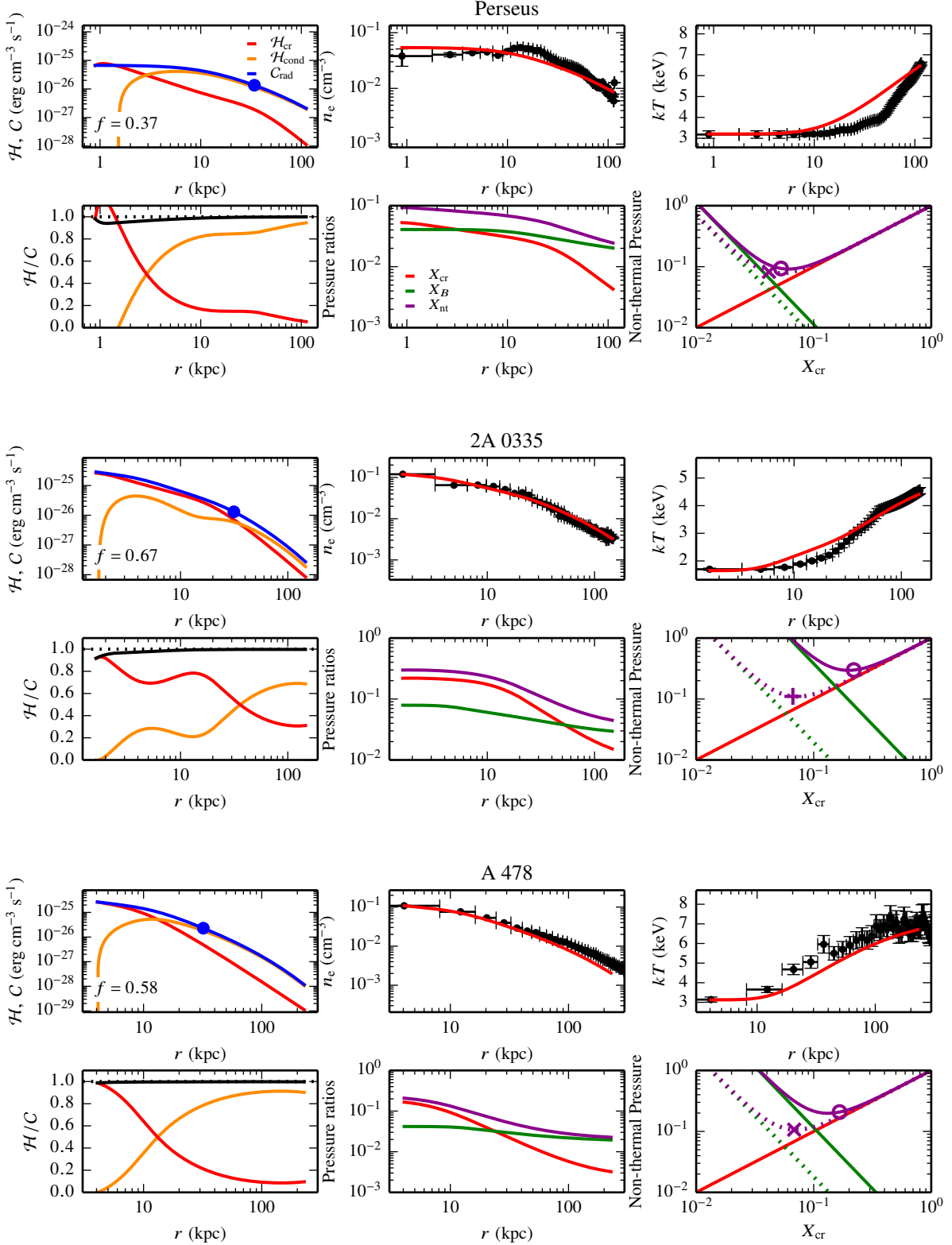


Figure A9. We show the same properties of the steady state solutions as in Fig. 4 for different clusters.

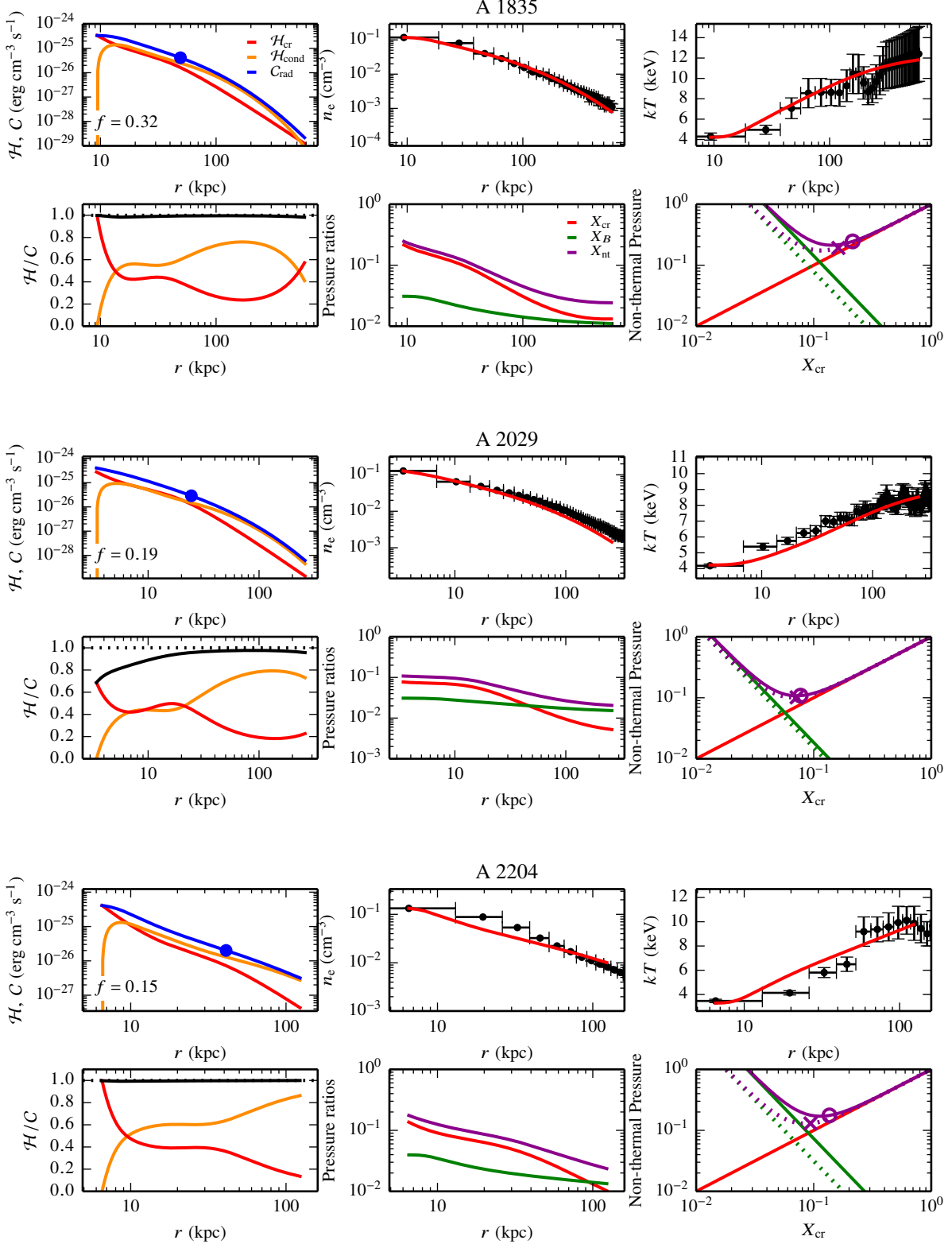


Figure A10. We show the same properties of the steady state solutions as in Fig. 4 for different clusters.

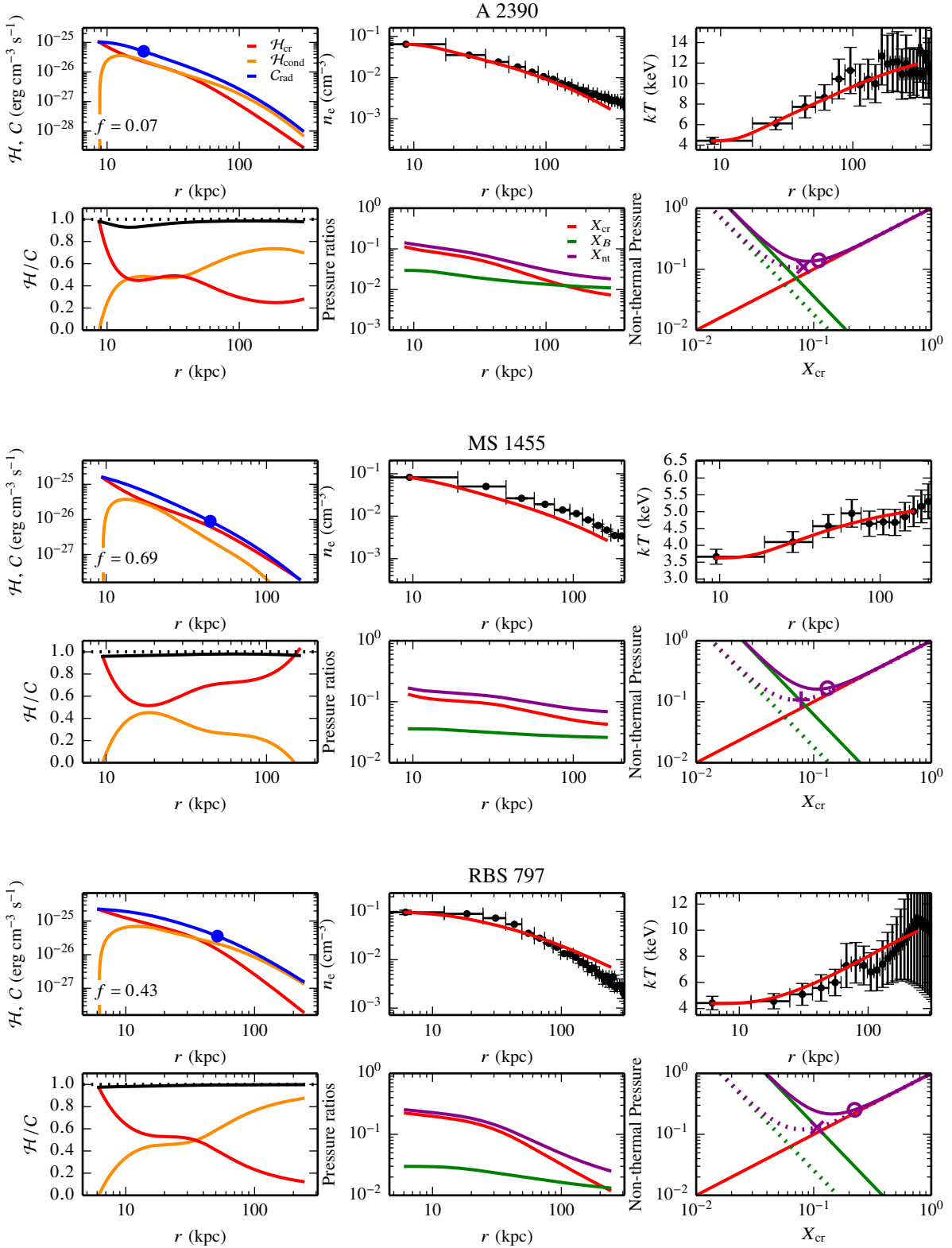


Figure A11. We show the same properties of the steady state solutions as in Fig. 4 for different clusters.

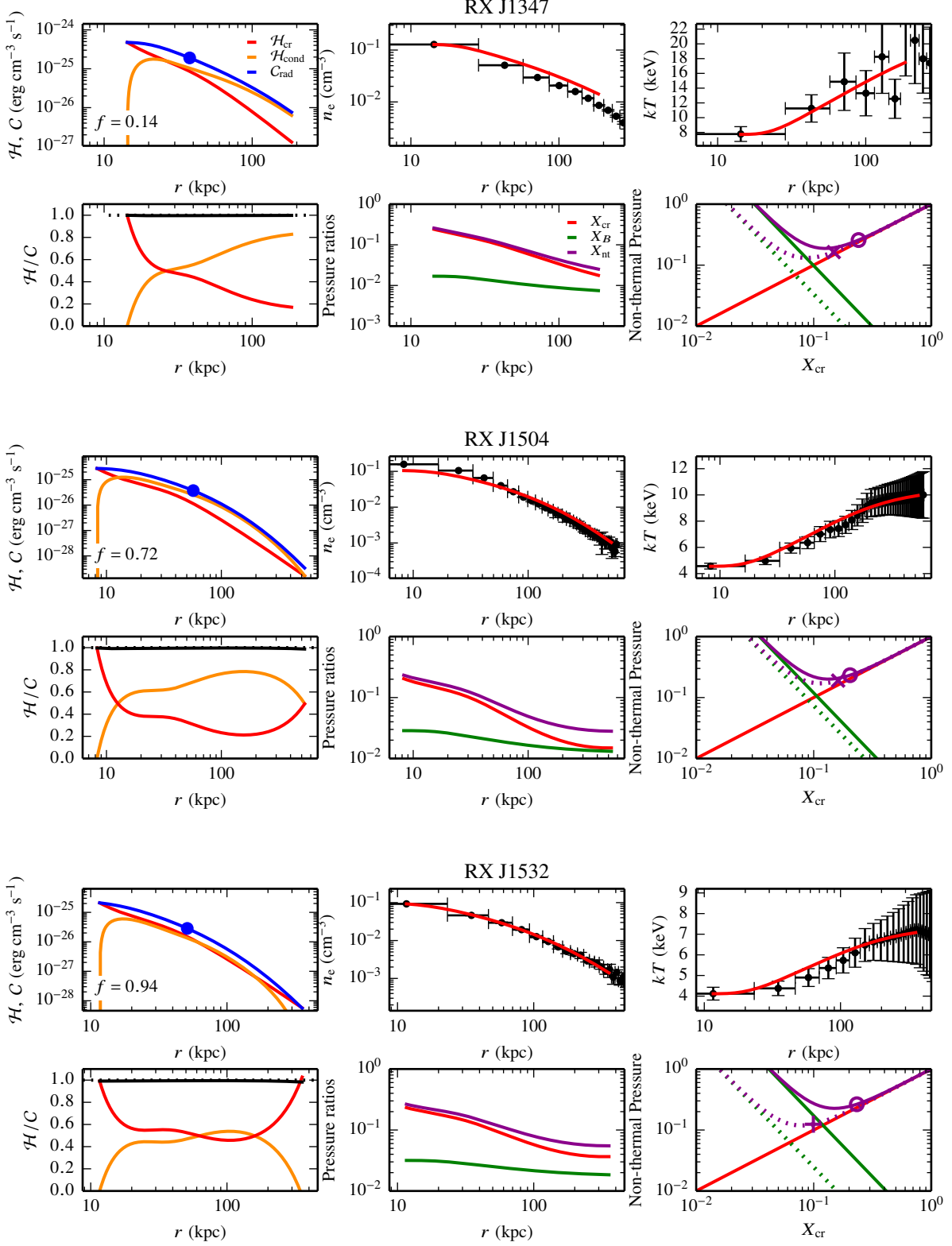


Figure A12. We show the same properties of the steady state solutions as in Fig. 4 for different clusters.

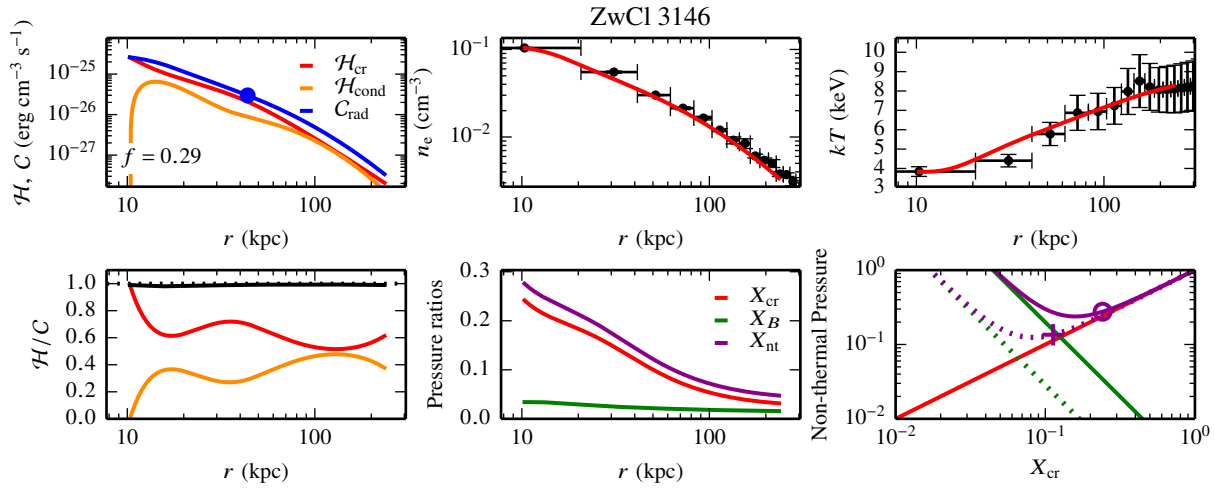


Figure A13. We show the same properties of the steady state solutions as in Fig. 4 for different clusters.

Table A1. Parameters for temperature profiles.

Cluster	$r_{\text{cut},T}^{(1)}$ kpc	$a^{(2)}$	T_0 keV	T_1 keV	r_T kpc	η
Centaurus	63	0.2	0.8	5.1	21	1.0
Hydra A	297	0.5	2.5	5.9	300 ⁽³⁾	0.5
Virgo	54	0.2	1.9	3.1	28	1.4
A 85	248	0.3	3.0	8.7	92	1.2
A 133	136	0.2	2.3	4.8	51	2.6
A 262	81	0.2	1.5	2.5	9	2.5
A 383	289	0.2	3.0	5.9	57	3.0
A 496	79	0.1	1.9	24.4	390	1.0
A 539	146	0.2	3.0	3.2	21	10.0
A 907	635	0.2	3.5	6.5	47	1.7
A 1644	292	0.2	2.0	5.5	49	1.5
A 1795	377	0.2	3.3	7.6	75	1.5
A 1991	197	0.2	0.9	3.0	19	1.5
A 2052	122	0.2	1.5	3.5	23	2.8
A 2199	104	0.1	2.7	4.9	24	2.1
A 2597	87	0.1	2.3	5.0	41	1.6
A 3112	245	0.2	2.7	5.7	35	1.6
A 3581	107	0.2	1.4	4.2	115	1.4
A 4059	221	0.2	2.1	5.0	30	2.0
AWM 7	78	0.2	2.6	3.8	14	2.5
MKW 3S	229	0.1	3.1	3.7	26	3.3
MKW 4	48	0.2	1.5	2.2	10	3.4
PKS 0745	416	0.5	3.2	20.0	300 ⁽³⁾	1.0
ZwCl 1742	343	0.2	3.0	4.3	51	6.1
Ophiuchus	257	0.2	0.8	9.3	14	1.1
Perseus	115	0.2	3.2	8.7	94	2.3
2A 0335	148	0.2	1.6	4.9	46	1.8
A 478	444	0.5	3.0	6.8	26	1.9
A 1835	590	0.4	2.6	17.	166	0.7
A 2029	497	0.2	1.7	14.7	121	0.4
A 2204	1040	0.2	3.3	10.2	40	3.0
A 2390	549	0.3	4.0	12.7	52	1.6
MS 1455	486	0.2	1.5	7.7	50 ⁽³⁾	0.4
RBS 797	315	0.5	4.2	15.2	217	1.2
RX J1347	501	0.08	6.6	23.8	82	1.5
RX J1504	587	0.5	4.4	10.9	105	1.4
RX J1532	477	0.4	4.1	7.6	108	2.0
RX J1720	367	0.4	4.4	7.5	86	2.7
ZwCl 3146	382	0.3	3.7	8.7	63	2.3

(1) Maximal radius that we include in fit.

(2) Parameter fixed in fit.

(3) Fixed value for r_T .